

The origin of boninites on Mercury: An experimental study of the northern volcanic plains lavas

Kathleen E. Vander Kaaden^{*}, Francis M. McCubbin

*Institute of Meteoritics, Department of Earth & Planetary Sciences, University of New Mexico, Albuquerque, NM 87131, USA
NASA Johnson Space Center, Mailcode X12, 2101 NASA Parkway, Houston, TX 77058, USA*

Received 11 March 2015; accepted in revised form 4 October 2015; available online 27 October 2015

Abstract

Phase equilibrium experiments were conducted on a synthetic rock composition matching that of the northern volcanic plains of Mercury as measured by the M^Ercury Surface, Space E^Nvironment, G^Eochemistry and Ranging spacecraft (MESSENGER). The northern volcanic plains are smooth plains of suspected volcanic origin that cover more than 6% of the surface area of Mercury. The northern volcanic plains are less cratered than their surroundings and reported to be the product of flood volcanism, making them a prime candidate for experimental study. The bulk composition of the northern volcanic plains is that of an alkali-rich boninite and represents the first silica-enriched crustal terrane identified on an extraterrestrial planet from orbital data. Phase equilibrium experiments were conducted over the pressure range of the mercurian mantle (0.5–5 GPa) at very low oxygen fugacity ($\sim \Delta IW_0$ to -7) using a piston-cylinder apparatus (P 0.5–1.7 GPa) and a Walker-style multi-anvil device ($P \geq 2.5$ GPa). Our results indicate the origin of the northern volcanic plains lavas (boninites) are best explained by high degrees of partial melting of an olivine-dominant, pyroxene- and plagioclase-bearing mantle source at low pressure (≤ 1.4 GPa) and does not require hydrous melting to achieve the silica-enriched melt composition. The formation mechanism for boninites on Mercury contrasts substantially with terrestrial boninites, which typically occur in oxidized and hydrous arc environments associated with subduction zones. Instead, mercurian boninites form at exceptionally low oxygen fugacity and do not require melting of hydrated source materials. The NVP lavas represent a novel mechanism by which planetary bodies can form silica-enriched secondary crusts without the aid of water.

© 2015 Elsevier Ltd. All rights reserved.

1. INTRODUCTION

With the recent estimates of Mercury's surface composition from the X-Ray Spectrometer (XRS) and Gamma-Ray Spectrometer (GRS) onboard the M^Ercury Surface, Space E^Nvironment, G^Eochemistry and Ranging (MESSENGER) spacecraft, we now have our first opportunity to directly investigate the compositions of lavas from the

planet Mercury and indirectly investigate the chemical make-up of Mercury's interior (Coffin and Eldholm, 1994; Nittler et al., 2011, 2013; Evans et al., 2012, 2015; Peplowski et al., 2012, 2014; Weider et al., 2012, 2014, 2015). Recent compositional information from Mercury's surface indicates high amounts of sulfur (up to 4 wt%) and relatively low amounts of iron (≤ 4 wt%) (Riner et al., 2010; Nittler et al., 2011; Peplowski et al., 2012; Weider et al., 2012), consistent with magmatism occurring under highly reducing conditions [i.e., 7–3 log₁₀ units below the iron–wüstite (IW) buffer] (McCubbin et al., 2012; Zolotov et al., 2013). Under such reducing conditions, one would expect the majority of the Fe within the planet to partition into the core. Although Fe has been detected on the surface

^{*} Corresponding author at: Institute of Meteoritics, Department of Earth & Planetary Sciences, University of New Mexico, Albuquerque, NM 87131, USA.

E-mail address: kvander@unm.edu (K.E. Vander Kaaden).

of Mercury, the low oxygen fugacity could indicate that the bulk of the iron on the surface is in the form of metallic iron and/or sulfides. XRS and GRS measurements of Mercury's surface from MESSENGER commonly have footprints that overlap several geologic terranes, so determining an appropriate melt composition for experimental study is a complicated process; however, the northern volcanic plains (NVP) on Mercury may represent an important exception.

The NVP are smooth plains of suspected volcanic origin that cover more than 6–7% of the surface area of Mercury (Head et al., 2011; Ostrach et al., 2015). Spanning a 4.7×10^6 to 10^7 km³ region of Mercury, this unit is less cratered than its surroundings and purported to be the product of flood volcanism (Head et al., 2011; Ostrach et al., 2015). Although there is some evidence that suggests this unit is not completely homogeneous (Peplowski et al., 2012; Weider et al., 2015), it is the largest volcanic province that has been assessed from orbit by MESSENGER. On Earth, flood volcanism is generally produced by partial melting of mantle material that is erupted onto the surface of the planet. The NVP region has previously been described as being similar to flood basalts and komatiites on Earth, based on similar Mg/Si, Al/Si, and Ca/Si ratios (Weider et al., 2012). The estimated volume of magma that composes the NVP (determined in Head et al., 2011; Ostrach et al., 2015) falls within the volume estimated for the terrestrial Deccan Lavas ($3\text{--}8.5 \times 10^6$ km³) and the Siberian Traps (4×10^6 km³), but the volume of the NVP is much greater than other large volcanic fields on Earth including the Karoo-Ferrar Province (0.3×10^6 km³) and the Columbia River Basalts ($0.175\text{--}1.3 \times 10^6$ km³) (Hooper and Hawkesworth, 1993; Coffin and Eldholm, 1994; Fedorenko et al., 1996, 2000; Peate, 1997; Takahashi et al., 1998; Sen, 2001). A schematic comparison of the

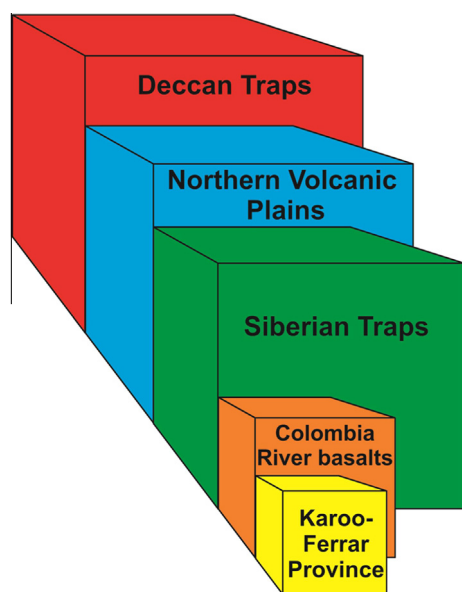


Fig. 1. Volume of lava produced from the northern volcanic plains magma compared to common voluminous terrestrial magmas (Hooper and Hawkesworth, 1993; Fedorenko et al., 1996, 2000; Peate, 1997; Takahashi et al., 1998; Sen, 2001). Boxes are to scale for the average amount of lava produced (refer to text).

average relative volumes of magma from each terrestrial flood volcanic province along with the NVP on Mercury is provided in Fig. 1. Flood volcanic provinces on Earth are generally tholeiitic in composition, require high degrees of partial melting, and melted at low pressure (2–4 GPa) (Hooper and Hawkesworth, 1993; Coffin and Eldholm, 1994; Fedorenko et al., 1996, 2000; Peate, 1997; Takahashi et al., 1998; Sen, 2001), although it is not yet clear whether these characteristics are applicable to flood volcanism on Mercury. In the present study, we experimentally investigate the high pressure phase equilibria of the NVP lavas to gain insight into their petrogenetic history, including source region mineralogy and possible depth and temperature of melting. However, before we conduct experimental work on the NVP lavas, we must first determine an appropriate composition for the NVP lavas as well as an appropriate petrologic characterization of that composition using the most recent XRS and GRS results from MESSENGER for the NVP region.

1.1. Composition and petrologic classification of the northern volcanic plains lavas

The most recent XRS and GRS footprints published by the MESSENGER team that specifically targeted the NVP region were used to determine an average composition of the NVP lavas. Specifically we used Mg/Si, Al/Si, Ca/Si, Fe/Si, and S/Si values from XRS reported in Weider et al. (2014), Na/Si values from GRS corresponding to 80–90°N latitude reported in Peplowski et al. (2014), and K values from GRS reported in Peplowski et al. (2012). The abundances of Ti, Mn, and Cr have not been reported for the NVP lavas; therefore we used the XRS detection limits for these elements reported by Nittler et al. (2011) as the upper limit concentrations of these elements.

In order to determine the composition of the NVP lavas from the elemental ratios reported by XRS, the absolute abundance of Si is required; however, the uncertainty on Si abundance measurements from GRS on Mercury is prohibitively high for determining precise surface compositions (i.e., $24.6 \pm 7\%$; Evans et al., 2012); therefore a model abundance of approximately 25% Si has typically been used (Nittler et al., 2011; Weider et al., 2012, 2014), which is within the uncertainty of GRS measurements of Si (Evans et al., 2012). Next, the valence of each element is assigned (i.e., Si⁴⁺, Ti⁴⁺, Al³⁺, Cr²⁺, Fe²⁺, Mn²⁺, Mg²⁺, Ca²⁺, Na⁺, K⁺, S²⁻) and a corresponding abundance of O²⁻ is determined such that the resulting composition is charge balanced. If the assumptions are valid and no major constituent elements were excluded, the resulting sum of oxides/sulfides should be near 100 wt%. However, the oxide/sulfide totals for the northern volcanic plains are low, even when the upper limit concentrations for Mn, Ti, and Cr are included (~95 wt%). Carbon and chlorine could make up some of this deficit given recently reported detections (or high minimum-detection limits in the case of C; Peplowski et al., 2015) from the MESSENGER GRS/NS instrument (Evans et al., 2015; Murchie et al., 2015; Peplowski et al., 2015); however there are no targeted analyses for C in the NVP region, and Cl abundances are

approximately 0.35 ± 0.13 wt% in the region of 80–90°N, which does little to make up the deficit in totals. Unless C abundances are at or near its three-sigma detection limit of 4.1 wt% in the NVP (Peplowski et al., 2015), it is unlikely that the deficiency in totals can be explained by any missing major elements in the NVP composition, so there is either a problem with the valence assignments or the model value for Si. Given that Mercury is a highly reduced planet, we first consider the valence assignments. Fe, Cr, and Ti all experience a change in valence state over the oxygen fugacity range exhibited by Mercury (Papike et al., 2005; McCubbin et al., 2012; Chabot et al., 2014); however, if Cr or Ti were assigned a lower valence, consistent with highly reducing conditions (Cr^{1+} and Ti^{3+}), the oxide/sulfide totals for the NVP lavas would only become lower. Furthermore, if Fe, Cr, and Ti are present as a metallic phase, they would not be a component in the silicate lavas, and the totals would be lower still. Additionally, metals exhibit limited solubility in silicate liquids and the large density contrast between metals and silicate liquids prohibits efficient transport of metals in silicate melts. Therefore, we rule out valence state assignments as the reason for low oxide/sulfide totals for the NVP lavas. Consequently, we have identified the calculated assumption of ~25 wt% Si as the reason for the low totals; therefore, we normalized the composition of the NVP lavas to 100%, while maintaining the measured Mg/Si, Al/Si, Ca/Si, Fe/Si, Na/Si, S/Si ratios. The resulting composition yielded computed Si abundances for the NVP of 26.2–26.8 wt% Si, which is within the measured value from MESSENGER GRS data of $24.6 \pm 7\%$ from Evans et al. (2012). We also computed an NVP composition without upper-limit estimates of Ti, Mn, and Cr, which will be implemented later when discussing possible sulfide mineralogy of the NVP lavas. Both NVP compositions are provided in Table 1.

The resulting bulk composition of the NVP lavas (Table 1) was classified petrologically according to International Union of Geological Sciences (IUGS) classification protocols (Le Maitre, 1984; Le Bas and Streckeisen, 1991; Le Bas, 2000; Le Maitre et al., 2002). This classification takes into account over three decades of consideration by an IUGS Subcommittee to ensure consistent terms are used across disciplines and planetary bodies when describing the chemical makeup of an igneous rock. We caution the reader that the classification determined here is based solely on chemical composition of the NVP lavas and it should not be used, *a priori*, to infer geologic processes or settings. The NVP lavas are metaluminous compositions with Mg#’s of ~96, an alkalinity index of 0.86, and ratio of non-bridging oxygen to tetrahedrally coordinated ions of 0.74–0.78 (Mysen, 1987). Using SiO_2 and total alkali content, both NVP compositions are intermediate trachyandesites on a total alkali vs. silica diagram (Le Maitre, 1984; Fig. 2). However, this diagram is not applicable to rocks with high MgO contents ($\text{MgO} > 8$ wt%, Le Bas and Streckeisen, 1991); consequently, in order to place further constraints on this classification, the High-Mg classification diagram (Fig. 2 in Le Bas, 2000) was employed. The average NVP composition plots in the boninite field with more than 8 wt% MgO and higher than 52 wt% SiO_2 . However, the total alkali content only extends to 4 wt%. Therefore, similar to alkali rich boninites on Earth, we have termed this composition an “alkalic boninite”. It is important to note that this composition does not fall in the komatiite field ($\text{MgO} > 18$ wt%, $\text{TiO}_2 < 1$ wt%, $\text{SiO}_2 < 52$ wt%, and alkalis < 1 wt%), which was also noted previously by Stockstill-Cahill et al. (2012), although their NVP composition included a lower estimated total alkali abundance (0.44 wt%).

Table 1

Composition of the silicate starting materials used in this study in wt% (Nittler et al., 2011, 2013; Weider et al., 2012; Peplowski et al., 2014).

	Average NVP*	Average NVP**	Alkali- and sulfur-free (NAS _F)	Alkali- and sulfur-bearing (NAS _B)	Equilibrated starting material (NSA-64)
SiO_2	57.37	56.11	57.76	54.09	57.03
TiO_2	0.00	0.81	1.35	1.26	1.14
Al_2O_3	13.98	13.68	13.47	12.61	11.63
CrO	0.00	0.69	0.71	0.66	0.11
FeO	1.03	1.01	5.21	0.00	0.06
MgO	15.56	15.22	15.22	14.26	16.67
MnO	0.00	0.68	0.69	0.65	0.52
CaO	4.20	4.11	5.58	5.23	5.90
Na_2O	7.16	7.01	0.00	6.82	5.03
K_2O	0.22	0.22	0.00	0.25	0.17
FeS	0.00	0.00	0.00	4.16	0.00
S^{2-}	0.94	0.92	0.00	0.00	1.31
Cl^-	0.00	0.00	0.00	0.00	1.40
$^-\text{O}=\text{S}+\text{Cl}$	0.46	0.47	0.00	0.00	0.97
Total	100.00	100.00	100.00	100.00	100.00

* Average composition without Cr, Ti, Mn.

** Average composition using upper limits for Cr, Ti, Mn.

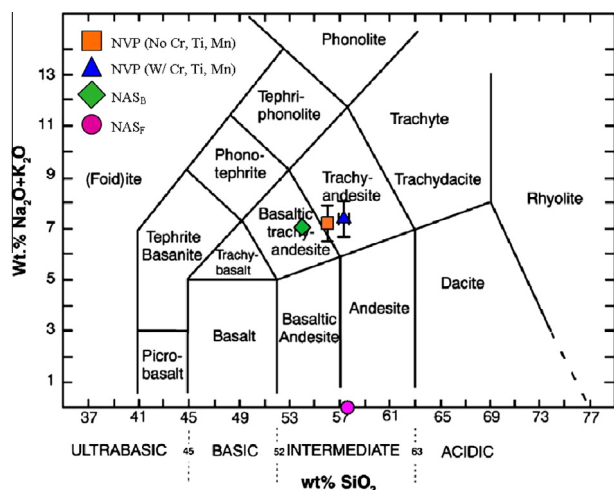


Fig. 2. Total alkali vs. silica diagram for the calculated NVP compositions as well as the experimental starting material used in this study.

CIPW (Cross, C.W., Iddings, J.P., Pirsson, L.W., and Washington, H.S.) norm calculations (Cross et al., 1903) were computed to determine the normative mineralogy of the NVP lavas (Table S1). The NVP lavas are nepheline normative and dominated by normative plagioclase, olivine, and pyroxene. The normative mineralogy was projected into the quartz, alkali feldspar, plagioclase feldspar, feldspathoid diagram for volcanic rock classification (Le Bas and Streckeisen, 1991), which classifies this composition as a basalt/andesite. Based on terrestrial criteria presented here, the NVP lavas can be classified as either Mg-rich trachyandesites or alkali-rich boninites. Importantly, this classification strongly depends on the amount of Si because this is the main element used to distinguish various rock types. Given the abundance of S in the NVP lavas, sulfide mineralogy cannot be determined from classical CIPW norm calculations, so we will rely on the experimental results in the present study to determine the relative partitioning of elements between the silicate and sulfide melt components and compute sulfide mineralogy prior to calculating CIPW norms on the residual, sulfide-removed compositions.

The presence of a geologic terrane on Mercury composed of rocks classified as either Mg-rich trachyandesites or alkali-rich boninites represents the first example of a silica-enriched crustal terrane that has been identified on the surface of an extraterrestrial body by remote sensing techniques. Although evolved lithologies have been identified from the Moon (Jolliff, 1991; Jolliff et al., 1999; Seddio et al., 2013), Mars (Stolper et al., 2013; Sautter et al., 2015; Santos et al., 2015), and asteroids (Day et al., 2009), these features have not been observed on scales that can be identified from orbit. On Earth, evolved crustal terranes, such as the continental crust, are reported to be a direct consequence of plate tectonics and the presence of H₂O (Campbell and Taylor, 1983); however plate tectonics is unlikely to have ever started on Mercury (Byrne et al., 2014), and the low oxygen fugacity of the planet

(McCubbin et al., 2012; Zolotov et al., 2013) would have resulted in H existing primarily as H₂ rather than H₂O (Sharp et al., 2013). The presence of the NVP on Mercury indicates that there are geologic processes that have operated to form silica-enriched crustal terranes in our Solar System that are unique from those that formed evolved crustal terranes on Earth. One of the goals of this study is to identify the geologic processes or conditions that led to the formation of such a silica-enriched crustal terrane on Mercury.

2. EXPERIMENTAL METHODS AND MOTIVATION

The primary goal of this experimental study is to use high pressure and temperature (*P–T*) phase relations of the best estimate of a melt composition from the mercurian surface to determine basic information about the planet's interior. Importantly, we stress that this kind of investigation has significant limitations given the methods by which the melt composition was determined. Although geologic evidence from remote observations supports the NVP lavas as a continuous unit of flood volcanism (Head et al., 2011; Denevi et al., 2013; Ostrach et al., 2015), we cannot assess, *a priori*, whether the lavas represent a primary unfractionated melt or a fractionated melt that was modified by earlier crystallization, which is typically assessed prior to experimental study. Furthermore, it has been recently suggested that the NVP lavas may not be homogeneous (Peplowski et al., 2012; Weider et al., 2015). Nevertheless, given that these experiments represent some of the first laboratory investigations of a suspected mercurian lava composition, these data will provide important first-order estimates of minimum average pressures and temperatures of melting as well as mantle mineralogy of Mercury, which is largely, at present, unconstrained. It will be difficult to use the experimental results here to provide firm constraints on the physical and chemical characteristics of the mercurian interior, so the results will be used to construct possible scenarios for the origin of the NVP lavas as well as possible characteristics of the mercurian interior. Fortunately, the shallow depth of Mercury's mantle ($\leq 420 \pm 30$ km; Hauck et al., 2013) provides a fairly limited pressure range (≤ 5 GPa) over which experiments need to be conducted. Consequently, we were able to investigate the entire *P–T* parameter space of the NVP phase diagram that is relevant to Mercury.

Experiments were conducted in the high pressure laboratory at the Institute of Meteoritics (IOM) at the University of New Mexico (UNM). Experiments in the pressure range of ~ 0.5 to 1.7 GPa were run in a 13 mm Depths of the Earth Quickpress™ non-end loaded piston cylinder (PC). A Walker style multi-anvil (MA) device was used for pressures from 2.5 to 5 GPa. Early reports from the MESSENGER team placed the sodium abundance on Mercury's surface at 2.9 ± 0.1 wt% Na (Evans et al., 2012). Additional data collection efforts have yielded better coverage of the planet and higher resolution measurements for Na, revealing substantial variations in Na across the surface of the planet. Peplowski et al. (2014) reported a range in Na content from ~ 5 wt% Na (i.e., 6.7 wt% Na₂O) in the

high northern latitudes on Mercury to ~ 2.6 wt% Na (i.e., 3.5 wt% Na_2O) near the equatorial regions. This large variation in Na will have important implications for the mineralogy of the mercurian surface because it's an important factor as to which side of the critical plane of silica saturation a melt composition lies (Yoder and Tilley, 1962; Irvine and Baragar, 1971; Peplowski et al., 2014). Consequently, in addition to the alkali- and S-bearing NVP composition (NAS_B) from Table 1, we also investigated a second melt composition with negligible alkalis and sulfur (NAS_F) (Table 1) to determine the effect on phase mineralogy if the elevated abundances of alkalis and S in the NVP were a consequence of thermal redistribution, which was initially proposed by Evans et al. (2013) but has since been ruled unlikely by Peplowski et al. (2014). The data from this alkali and sulfur free composition will also allow for extrapolation of our dataset to areas on Mercury that are not as high in alkali and S components as the NVP. However, since recent MESSENGER results suggest high abundances of alkalis and S, we primarily focus here on the phase equilibrium results from the NAS_B composition from Table 1, although the experimental results on the NAS_F composition are also provided and discussed where relevant.

2.1. Starting materials

The synthetic starting materials (Table 1) for the two NVP compositions (NAS_F and NAS_B) investigated in this study were prepared at the IOM using high-purity reagent grade powdered oxides, silicates, and sulfides, which were mixed sequentially by increasing volume and ground under ethanol using an automated agate mortar and pestle. For the NAS_F mix, all the Fe was added as FeO in the form of synthetic fayalite. The reader is referred to Vander Kaaden et al. (2015) for details regarding the preparation of the synthetic fayalite. For the NAS_B , all the Fe was added as FeS. The starting materials were allowed to dry completely and kept in either a desiccator or a drying oven at 100 °C before use in each experiment.

2.2. Phase equilibrium experiments

2.2.1. Capsule materials and oxygen fugacity

The NAS_F experiments did not present the same challenges as the NAS_B composition in terms of determining an appropriate capsule material. Without the worry of S to react with metal, these experiments were run in molybdenum capsules, which control the oxygen fugacity to within a few \log_{10} units of the iron-wüstite (IW) buffer over the P – T range of our experiments (O'Neill, 1986; Burkemper et al., 2012). Although the oxygen fugacity of the NAS_F experiments is not as low as the mercurian interior or the NAS_B experiments, it is sufficiently low to assess the mineralogical differences between the two starting compositions. However, we caution that temperatures and pressures of multiple saturation points determined from the NAS_F composition should shift slightly if run at more appropriate oxygen fugacity, which has been demonstrated experimentally in lunar magma compositions (i.e., Krawczynski and Grove, 2012).

Careful consideration of capsule material was required for running the NAS_B experiments because we needed a capsule that would not react with the melt components, including sulfur, so many metal capsule materials (Mo^0 and Fe^0) were ruled out due to their demonstrated affinity for sulfur (e.g., Tauster et al., 1980). Additionally, sulfur solubility increases in silicate melts with decreasing oxygen fugacity (Mavrogenes and O'Neill, 1999; McCoy et al., 1999; Holzheid and Grove, 2002; Malavergne et al., 2007, 2014; Berthet et al., 2009; Moune et al., 2009; Beermann et al., 2011; Zolotov et al., 2013), so the experiments were run under low oxygen fugacity to promote S-dissolution into the silicate melt. Furthermore, McCubbin et al. (2012) and Zolotov et al. (2013) have shown the oxygen fugacity of Mercury is between 7 and 3 \log_{10} units below the IW buffer, so highly reducing conditions provide a more realistic representation of the interior of Mercury. Graphite minimally reacts with silicate liquids especially under reducing conditions (Ardia et al., 2013), so it was chosen as the capsule material for the NAS_B experiments. Graphite capsules are incapable of controlling oxygen fugacity much below the graphite-CO buffer, so we needed to add an additional component to the experiments to promote reducing conditions. Consequently, oxygen fugacity was lowered in each experimental charge by adding Si metal to the bottom of each capsule in an $\sim 1:2$ mixture of Si metal:silicate starting material (Table 1), similar to the procedure of Siebert et al. (2004) and Rose-Weston et al. (2009). Therefore, these experiments were within a \log_{10} unit of the Si– SiO_2 oxygen fugacity buffer, which is within the range reported for Mercury over the temperature range of our experiments.

2.2.2. Piston cylinder experiments

Experiments for pressures ≤ 1.7 GPa were run in the PC using the procedures, parts, and calibrations described previously in Vander Kaaden et al. (2015) and McCubbin et al. (2015), although we briefly summarize the setup here. The loaded capsules were placed within salt-pyrex cells, which were used as a pressure medium, with crushable MgO parts and a graphite furnace. Exceptions to the procedure include using run durations from 4 to 21 h and using a Type B ($\text{Pt}_{30}\text{Rh}_{70}/\text{Pt}_{6}\text{Rh}_{94}$) thermocouple and Eurotherm (2416) controller to control and monitor temperature throughout the duration of each run. Each experiment was quenched by shutting off power to the furnace and slowly decompressing the run. Experiments on the NAS_F composition were run at 0.57 and 1.2 GPa in the temperature range of 1300–1450 °C, with run durations of 0.25–4 h. NAS_B experiments were run at pressures of 0.57–1.7 GPa between 1100 and 1480 °C, with run durations of 4–21 h. When possible, charges were taken to superliquidus temperatures for 3–20 min, depending on the stability of the assembly at a given temperature and pressure before dropping to the crystallization temperature.

2.2.3. Multi-anvil experiments

Experiments run at pressures between 2.5 and 5 GPa were performed in a MA using procedures that are identical to those described in Vander Kaaden et al. (2015), including a ceramic octahedron, Al_2O_3 inner parts, and 8 mm

truncation-edge-length of tungsten carbide cubes. The reader is referred to Agee et al. (1995) for our MA pressure calibration data and procedures. At the termination of each run, the charge was quenched and slowly decompressed in the same manner as the PC experiments. Experiments on the NAS_F composition were run at pressures from 3.5 to 5 GPa in the temperature range of 1350–2000 °C, with run durations of 1–3 h. NAS_B experiments were run at pressures ranging from 2.5 to 5 GPa between 1600 and 1950 °C, with run durations of 4 h. Similarly to PC experiments, charges were taken to superliquidus temperatures when possible for 3.5–18 min, depending on the stability of the assembly at a given temperature and pressure before dropping to the crystallization temperature.

2.2.4. Approach to a steady-state

Under the highly reducing conditions of our experimental runs, typical exchange coefficients for Mg and Fe between olivine and liquid ($K_{\text{DOI-Liq}}^{\text{Mg-Fe}}$) cannot be accurately calculated to assess equilibrium within these experiments due to the low amount of Fe in our starting composition. Furthermore, the majority of the Fe in our starting materials partitions into the metal or sulfide phases resulting in low FeO (0.02–0.24 wt%) in the melt. The homogeneous nature of each experimental charge, however, does suggest that our experiments approached a steady-state during our 2–24 h run durations. Furthermore, there were no

inconsistencies in our data to suggest the experimental charges required additional time to equilibrate, and all of the olivine present are consistently Fo₁₀₀.

In order to provide an additional check on steady-state conditions, we performed a time series using the NAS_B + Si metal compositions. Care was taken when filling the capsules to ensure equal portions of the NAS_B silicate starting composition and Si metal were loaded into each capsule so the experiments could be directly compared. Experiments were run at 1 GPa and 1425 °C for 0.3, 1.5, 4, 11, and 22 h. Analyses of these experiments show an increase in SiO₂ with increasing run time (Fig. S1). There is little difference between the 1.5 and 4 h run durations for SiO₂, however, there is a >1 wt% increase in SiO₂ after holding the run for 11 h and >6 wt% increases after holding for 22 h when compared with the 4 h run duration. A crystalline SiO₂ phase was present in the time-series runs that were held for 11 and 22 h, indicating that our system was susceptible to O diffusion into the capsule, which reacted with the Si metal to raise the SiO₂ content of the melt. Evidence of O diffusion was also observed in a subset of experiments with similar starting materials not included in this work (Fig. 3B) where olivine cores were present within pyroxene grains for experiments longer than 4–10 h. Consequently, caution was taken for any interpretations of our data that were highly dependent on silica activity, including the olivine-opx cotectic point along the liquidus, which we ver-

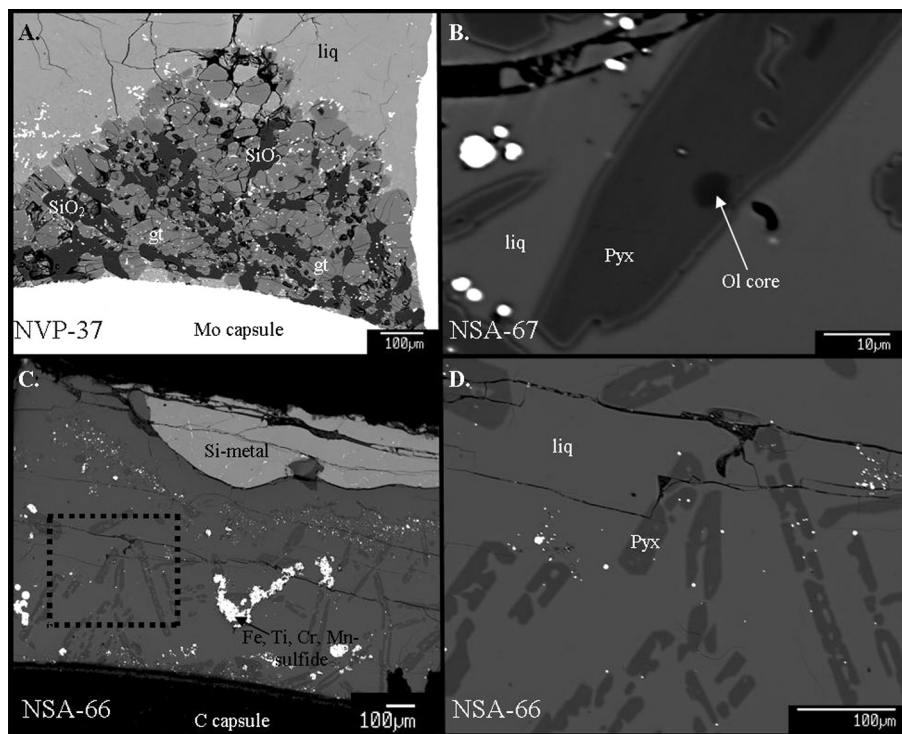


Fig. 3. Backscattered electron images of select experimental run products. (A) Experimental charge from the NAS_F composition (5 GPa, 1975 °C, 2 h). (B) Experimental charge from a subset of experiments not included in this study showing the result of oxygen diffusion into the capsule for experiments with run durations of longer than 4 h (0.9 GPa, 1300 °C, 5 h). (C) Experimental charge from the NAS_B composition (1.7 GPa, 1360 °C, 4 h). (D) A zoomed-in image of the dotted rectangular box in (C). Liq: liquid, SiO₂: silica phase, gt: garnet, pyx: pyroxene, ol: olivine, Mo: molybdenum capsule, C: graphite capsule.

ified using shorter (≤ 4 h) run durations. The FeO content in the melt decreased until 4 h and remained fairly constant in the longer run durations (Fig. S1) indicating that redox equilibrium was reached by 4 h. TiO_2 content also decreased over time and S^{2-} increased with increasing run duration.

We also compared the run products from experiments with and without a super-liquidus step as an additional check on whether or not our experiments reached a steady-state. Experiment NSA-34 was taken directly to its crystallization temperature of 1300°C and held for 4 h. This experiment consisted of olivine and melt. We then ran experiment NSA-59, which was first taken to a superliquidus temperature of 1425°C for ~ 20 min before being dropped to the crystallization temperature of 1300°C , and it was held for 24 h. The results of NSA-59 also consisted of olivine and melt, although the melt composition of NSA-59 had slightly higher SiO_2 , which was expected from the O diffusion problem discussed above. The results of these experiments as well as the homogeneous nature of our run products and lack of discrepancies along our phase diagram support our experiments reaching a steady state within the duration of the runs.

3. ANALYTICAL TECHNIQUES

Each experimental charge was ground and polished to expose the maximum surface area and all phases present. All NAS_F run products were polished using water as the lubricating material. However, Murthy et al. (2003) have shown loss of K from the FeS phase within their run products when using oil- or water-based lubricants during polishing. Furthermore, we analyzed multiple NAS_B experiments by electron probe microanalysis (EPMA) before and after treatment with water and acetone, and the silicate glasses had lower abundances (0.2–1.2 wt%) of volatile elements (mainly Na_2O , S^{2-} , and Cl^-) after treatment (Fig. S2). Therefore, all of our NAS_B experimental charges were polished dry using hexagonal boron nitride as a lubricant, which we mixed with various grit sizes of alumina powder. All experimental charges were polished to a $0.3\ \mu\text{m}$ finish.

3.1. Electron probe microanalysis

All phases present in each experiment were analyzed using a JEOL JXA 8200 electron microprobe housed in the IOM at UNM. Silicates, metals, and sulfides were analyzed using an accelerating voltage of 15 keV. A beam current of 15 nA was used for silicates whereas metals and sulfides were analyzed using a beam current of 20 nA. A broad beam ($10\text{--}20\ \mu\text{m}$) was used for glass analyses and a focused beam ($1\text{--}5\ \mu\text{m}$) was used for silicate minerals, metals, and sulfides. The standards albite (for Na), almandine (Al, Fe), augite (Si, Al, Ca, Mg), olivine (Mg, Si, Fe), orthoclase (K), pyrope (Cr, Mg, Ca), titanite (Ti), and spessartine (Mn) were used to analyze our quenched melt and silicate minerals. A sodalite standard was used to determine the amount of Cl^- contamination and a synthetic CaMoO_4 was used to determine the amount of MoO_2 contamination

in the glasses for the NAS_F runs. Metal and sulfide standards included Al-metal, albite (for Na), Cr-metal, orthoclase (K), Si metal, pyrite and troilite (S), Mg-metal, spessartine (Mn), augite (Ca), Fe-metal, Ti-metal, and sodalite (Cl). Peak positions were checked on the silicate standards used for metal and sulfide analyses and compared with the peak position of the experimental charge to ensure that analyses were conducted at the correct peak position. Peak count times ranged from 30 to 60 s and background count times ranged from 15 to 30 s, respectively. Analyses in the proximity of Si-rich metal typically suffered from substantial secondary fluorescence of Si, resulting in elevated totals and elevated abundances of Si, so care was taken to measure glass that was $\geq 200\ \mu\text{m}$ from the Si metal.

3.2. Micro-Fourier transform infrared spectroscopy (FTIR)

The presence of H_2O can substantially depress the liquidus temperature of basaltic melts (e.g., Médard and Grove, 2008), so quantitative infrared spectroscopic measurements were conducted on the experimental glass products of numerous experimental charges at room temperature in transmittance mode with a Nicolet Nexus 670 Fourier Transform Infrared Spectrometer in the IOM at UNM to determine the amount of H_2O present in the “dry” runs from this study. Transmittance IR spectra were collected from doubly polished wafers of the run products over the mid-IR range ($400\text{--}4000\ \text{cm}^{-1}$) using a Continuum microscope with a Globar source, XT-KBr beamsplitter, and a MCT/A detector over a $100 \times 100\ \mu\text{m}$ area with a $4\ \text{cm}^{-1}$ resolution. Thicknesses for each sample were obtained by focusing a reflected aperture on the top surface of the sample first then the bottom surface of the sample and recording the z -axis position of the mapping stage in the Atlas software. These arbitrary units were converted to micrometers using a previous calibration (Berger, 2012). Background spectra were collected under the same conditions before each analysis. Total dissolved water concentrations were determined for each glass from the intensity of the broad band at $3570\ \text{cm}^{-1}$ after the calculation scheme of Mandeville et al. (2002) and Dixon et al. (1995). One thousand and twenty-four scans were performed for each IR spectrum acquired. The reader is referred to Vander Kaaden et al. (2015) for full details on this procedure.

4. CALCULATIONS OF OXYGEN FUGACITY

The oxygen fugacity of all experiments that were sulfur and alkali free (NAS_F) was controlled through the starting material composition as well as the molybdenum capsule that was used in each experiment. Due to the low solubility of MoO_2 in silicate melts (Table S2 and Burkemper et al., 2012) and the presence of the Mo capsule, we can constrain the $f\text{O}_2$ of each experiment to being at or below the Mo– MoO_2 buffer. In order to attempt to quantify the $f\text{O}_2$ of each experimental run product after the analysis of each experiment by EPMA, the oxygen fugacity of the charge was calculated using the melt phase present in the experi-

ment and assuming an activity of one for Fe metal. This approach gives us a minimum value for the f_{O_2} of each experiment relative to the IW buffer. Using these two phases, the oxygen fugacity of the charge was calculated relative to the IW buffer using Eq. (1).

$$\Delta \text{IW} = 2 \log \left(\frac{x_{\text{FeO}}^{\text{silicate}} * \gamma_{\text{FeO}}^{\text{silicate}}}{x_{\text{Fe}}^{\text{metal}} * \gamma_{\text{Fe}}^{\text{metal}}} \right) \quad (1)$$

where $x_{\text{FeO}}^{\text{silicate}}$ is the mole fraction of FeO in the silicate, $\gamma_{\text{FeO}}^{\text{silicate}}$ is the activity coefficient of FeO in the silicate, $x_{\text{Fe}}^{\text{metal}}$ is the mole fraction of Fe in the metal, and $\gamma_{\text{Fe}}^{\text{metal}}$ is the activity coefficient of Fe in the metal. To begin, we assume ideality to make a first-order approximation of the oxygen fugacity (see also below). Since we are assuming that a pure Fe-metal phase is present, the activity of Fe in the metal is fixed at unity. The f_{O_2} of every NAS_{F} experiment was calculated, where melt was present, resulting in f_{O_2} values of 2.24–2.76 \log_{10} units below the IW buffer. Since there was not an Fe-metal phase present in any of our experiments, the experimental charges are likely to be more oxidizing than this estimate. Using this constraint on the lower bound of f_{O_2} and the fact that the Mo–MoO₂ and IW buffer are essentially equal at the P – T conditions of interest (Burkemper et al., 2012), the oxygen fugacity of our NAS_{F} experiments lies somewhere between IW and IW-2.76. The estimated f_{O_2} of each experiment is given in Table 2.

The oxygen fugacity of all experiments containing sulfur was controlled through the addition of Si metal to each individual capsule. After the analysis of each experiment, the oxygen fugacity of the charge was calculated two different ways. First, the f_{O_2} was calculated relative to the Si–SiO₂ buffer using Eq. (2).

$$\Delta \text{Si–SiO}_2 = \log \left(\frac{x_{\text{SiO}_2}^{\text{silicate}} * \gamma_{\text{SiO}_2}^{\text{silicate}}}{x_{\text{Si}}^{\text{metal}} * \gamma_{\text{Si}}^{\text{metal}}} \right) \quad (2)$$

where $x_{\text{SiO}_2}^{\text{silicate}}$ is the mole fraction of SiO₂ in the silicate, $\gamma_{\text{SiO}_2}^{\text{silicate}}$ is the activity coefficient for SiO₂ in the silicate, $x_{\text{Si}}^{\text{metal}}$ is the mole fraction of Si in the metal, and $\gamma_{\text{Si}}^{\text{metal}}$ is the activity coefficient for Si in the metal. Similar to the method above, we begin by assuming ideality to make a first-order approximation of the oxygen fugacity. However, the presence of Si metal in each experiment fixed the Si activity to unity, so only the activity coefficient for SiO₂ is uncertain. The f_{O_2} of every NAS_{B} experiment was calculated, where melt was present, using the melt phase and the Si-rich metal phase resulting in f_{O_2} values of 0.17–0.27 \log_{10} units below the Si–SiO₂ buffer. A second calculation of oxygen fugacity was conducted using the same melt and an Fe-rich metal phase, when present. Using these two phases, the oxygen fugacity of the charge was calculated relative to the iron-wüstite buffer using Eq. (1). We begin again by assuming ideality to make a first-order approximation of the oxygen fugacity. These calculations resulted in oxygen fugacities between 5.45 and 6.86 \log_{10} units below the IW buffer, which is more reducing than the NAS_{F} experiments by ~ 3 to 7 \log_{10} units. Both calculations (using Eqs. (1) and (2)) for a given experiment typically agreed within approximately 1 \log_{10} unit, indicating that ideality

is a valid assumption for a first-order approximation of the oxygen fugacity. The f_{O_2} of each experiment is given in Table 2.

We have also gone through the exercise of calculating activity coefficients for FeO (O'Neill and Eggins, 2002), SiO₂ (Carmichael et al., 1970; Beattie, 1993), Fe⁰, and Si⁰ (Wade and Wood, 2005) and performing the same calculations given in Eqs. (1) and (2). Although the majority of our results shifted only by $\leq 0.5 \log_{10}$ units in either direction, in a few cases these calculations resulted in values considered to be erroneous (e.g., $\Delta \text{IW} + 15.91$ for NSA-10 and $\Delta \text{Si–SiO}_2 - 18.44$ for NSA-21). For this reason we have chosen to compute all f_{O_2} values in this manuscript assuming ideality. This assumption, although not strictly correct, is considered to introduce the least amount of scatter in the precision of our estimates of oxygen fugacity, although there may be up to a 0.5 \log_{10} units uncertainty in accuracy.

5. RESULTS

Table 2 includes a full listing of experiments conducted for NAS_{F} and NAS_{B} compositions along with the run conditions, phases present, and estimated oxygen fugacity. The results of each experiment in this study including capsule material, run conditions, run durations, oxygen fugacity, and EPMA data can be found in the [Supplementary Materials](#) (Tables S2–S4). Backscattered electron images of representative experimental charges are shown in Fig. 3.

5.1. NAS_{B} phase equilibrium experiments

The phase diagram for the NAS_{B} composition is shown in Fig. 4. SiC was present in most experimental run products at the boundary of the graphite capsule and Si metal, but was much more prominent in MA experiments. Where grains were large enough, analyses were conducted (Table S3) and the carbon abundance was calculated by difference. In this alkali- and sulfur-bearing system, forsterite is the liquidus phase at low pressures (<1.4 GPa) between ~ 1250 and ~ 1600 °C and albitic plagioclase is present at 0.57 GPa and 1100 °C. A multiple saturation point (MSP) occurs when two or more minerals coexist at the same point in P – T space along the liquidus. The first MSP occurs at ~ 1.4 GPa and ~ 1460 °C between olivine and orthopyroxene. At pressures between 1.4 and 2.7 GPa, enstatite-rich pyroxene is the liquidus phase. A second MSP occurs at ~ 2.7 GPa and ~ 1640 °C between orthopyroxene and a jadeite-like pyroxene. The composition of this jadeite-like pyroxene is $\text{En}_{89}\text{Wo}_{11}$ and has ~ 3 wt% Na₂O in its structure. At pressures greater than ~ 3.8 GPa and ~ 1800 °C, silica appears as a liquidus phase with a jadeite-like pyroxene (~ 6 to 7 wt% Na₂O). However, the appearance of SiO₂ on the liquidus is most likely a direct effect of O diffusion into our capsule reacting with the Si metal used to reduce the experiments. Consequently, we cannot confirm the validity of silica on the high pressure liquidus of the NAS_{B} composition.

The compositions of the residual melts (Table S3) vary as a function of pressure, temperature, and mineral phases present. They are consistently high in SiO₂ (56.86–67.74 wt

Table 2

Table of experimental run conditions and results.

Run	Capsule	<i>P</i> (GPa)	Superliq (°C)	Superliq (min)	<i>T</i> (°C)	Duration (h)	Phase assemblage	$\Delta I W^*$	$\Delta Si-SiO_2^\dagger$
NVP-45	Mo ⁰	0.57	—	—	1300	2	Lq, En ₉₀ Fs ₈ Wo ₂ , SiO ₂	−2.67 [^]	—
NVP-40	Mo ⁰	0.57	—	—	1360	0.375	Lq, En ₉₁ Fs ₇ Wo ₂ , SiO ₂	−2.71 [^]	—
NVP-42	Mo ⁰	0.57	—	—	1375	1.05	Lq	−2.73 [^]	—
NVP-20	Mo ⁰	1.2	—	—	1350	2	Lq, En ₈₉ Fs ₉ Wo ₂ , SiO ₂	−2.66 [^]	—
NVP-10	Mo ⁰	3	—	—	1700	1	Lq, En ₉₀ Fs ₂ Wo ₈ , SiO ₂ , Py ₈₂ Al ₁₁ Gr ₇	−2.69 [^]	—
NVP-14	Mo ⁰	3	—	—	1800	1	Liq	−2.75 [^]	—
NVP-44	Mo ⁰	3.5	—	—	1350	3	En ₈₇ Fs ₁₀ Wo ₃ , SiO ₂ , Py ₆₉ Al ₁₇ Gr ₁₄	—	—
NVP-27	Mo ⁰	3.5	—	—	1800	2	Lq, Py ₈₂ Al ₁₁ Gr ₇ , SiO ₂	−2.56 [^]	—
NVP-29	Mo ⁰	3.5	—	—	1875	2	Lq, Py ₈₅ Al ₁₀ Gr ₅ , SiO ₂	−2.72 [^]	—
NVP-21	Mo ⁰	4	—	—	1800	2	Lq, Py ₈₂ Al ₁₁ Gr ₇ , SiO ₂	−2.55 [^]	—
NVP-26	Mo ⁰	4	—	—	1850	2	Lq, Py ₈₄ Al ₁₀ Gr ₆ , SiO ₂	−2.65 [^]	—
NVP-31	Mo ⁰	4	—	—	1900	2	Lq, Py ₈₅ Al ₁₀ Gr ₅ , SiO ₂	−2.66 [^]	—
NVP-35	Mo ⁰	4	—	—	1950	2	Lq	−2.74 [^]	—
NVP-15	Mo ⁰	5	—	—	1850	2	Lq, En ₆₆ Fs ₉ Wo ₂₅ , Py ₇₄ Al ₁₃ Gr ₁₃ , SiO ₂	−2.24 [^]	—
NVP-17	Mo ⁰	5	—	—	1950	2	Lq, Py ₈₅ Al ₁₀ Gr ₆ , SiO ₂	−2.70 [^]	—
NVP-37	Mo ⁰	5	—	—	1975	2	Lq, Py ₈₁ Al ₁₁ Gr ₈ , SiO ₂	−2.62 [^]	—
NVP-22	Mo ⁰	5	—	—	2000	2	Liq	−2.76 [^]	—
NSA-11	C	0.57	1300	18	1100	4	Plg, En-rich, Mtl, Sfd	—	—
NSA-14	C	0.57	1350	4	1200	24	Lq, Fo ₁₀₀ , SiC, Mtl, Sfd	−6.57	−0.20
NSA-34	C	0.57	—	—	1300	4	Lq, Fo _{99.5} Fa _{0.5} , Mtl, Sfd	—	−0.21
NSA-64	C	1.0	—	—	1425	4	Lq, Mtl	—	−0.27
NSA-23	C	1.2	—	—	1300	21.7	Lq, En ₉₆ Fs ₁ Wo ₃ , Mtl, Sfd	—	−0.21
NSA-25	C	1.2	—	—	1325	8	Lq, Fo ₁₀₀ , En ₉₇ Fs ₀ Wo ₃ , SiC, Mtl	−6.86	−0.23
NSA-27	C	1.2	—	—	1400	4	Lq, Fo-rich, SiC, Mtl	−6.94	−0.21
NSA-66	C	1.7	1450	60	1360	4	Lq, En ₉₇ Fs ₁ Wo ₂ , Mtl, Sfd	—	−0.24
NSA-65	C	1.7	1450	0.3	1380	24	Lq, En ₉₇ Fs ₁ Wo ₂ , Mtl, Sfd	—	−0.21
NSA-71	C	1.7	—	—	1450	4	Lq, En ₉₇ Fs ₁ Wo ₂ , Mtl	−5.29	−0.26
NSA-70	C	1.7	—	—	1480	4	Lq, Mtl, Sfd	—	−0.22
NSA-36	C	2.5	—	—	1450	4	Lq, En ₈₅ Fs ₂ Wo ₁₃ , SiO ₂ , Mtl, Sfd	−5.66	−0.15
NSA-29	C	2.5	—	—	1600	4	Lq, En ₉₇ Fs ₀ Wo ₃ , SiC, Mtl	−6.33	−0.19
NSA-13	C	3	1700	10	1400	4	Lq, En ₈₅ Fs ₀ Wo ₁₅ , SiO ₂ , SiC, Mtl, Sfd	—	−0.13
NSA-21	C	3	1750	10	1600	4	Lq, En ₈₉ Fs ₀ Wo ₁₁ , SiC, Mtl	−6.34	−0.18
NSA-10	C	3	1700	10	1500	4	Lq, En ₈₈ Fs ₀ Wo ₁₂ , En ₈₁ Fs ₀ Wo ₁₉ , SiO ₂ , SiC, Mtl, Sfd	−5.28	−0.13
NSA-17	C	3	1800	3.5	1700	4	Lq, SiC, Mtl	−5.75	−0.18
NSA-9	C	4	1750	10	1550	4	En ₈₂ Fs ₀ Wo ₁₈ , SiO ₂ , SiC, Mtl, Sfd	—	0.00
NSA-8	C	4	1750	10	1650	4	Lq, En ₇₉ Fs ₂ Wo ₁₉ , SiO ₂ , SiC, Mtl, Sfd	—	0.00
NSA-15	C	4	1950	10	1750	4	Lq, En ₈₂ Fs ₀ Wo ₁₈ , SiO ₂ , SiC, Mtl, Sfd	−7.05	−0.19
NSA-12	C	5	1850	10	1650	4	En ₇₈ Fs ₃ Wo ₁₉ , SiO ₂ , Mtl, Sfd	—	0.00
NSA-24	C	5	1850	10	1750	4	En ₈₀ Fs ₂ Wo ₁₈ , SiO ₂ , SiC, Mtl, Sfd	—	0.00
NSA-28	C	5	1900	10	1850	4	Lq, En ₈₁ Fs ₁ Wo ₁₈ , SiO ₂ , SiC, Mtl, Sfd	—	0.00
NSA-18	C	5	1900	3.5	—	—	Lq, SiC, Mtl	−6.79	−0.22

Abbreviations are as follows: Liquid (lq), Plagioclase (Plg), Olivine (ol) Pyroxene (pyx), Garnet (gt), Silicon Carbide (SiC), Metals (Mtl), Sulfides (Sfd).

* Oxygen fugacity calculated using Fe-rich metal.

† Oxygen fugacity calculated using Si-rich metal.

^ Oxygen fugacity is more oxidizing than this value.

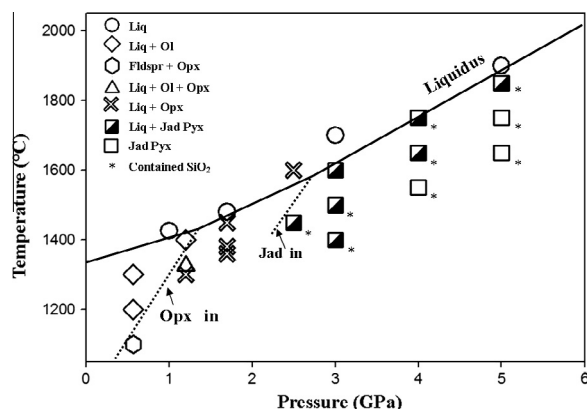


Fig. 4. Experimental phase diagram for the NAS_B composition. The solid black line is the liquidus for this composition. The dotted lines are estimated mineral-in lines. Each phase is identified by a different symbol. There is a multiple saturation point between olivine and orthopyroxene at ~ 1.4 GPa and a multiple saturation point between orthopyroxene and jadeite-like pyroxene at ~ 2.7 GPa. The appearance of SiO_2 is most likely the result of O diffusion into our capsule reacting with Si metal. The liquidus line is anchored at the 1-bar liquidus temperature from [Schlke and Whittington \(2015\)](#).

%, extremely low in FeO (0.02–0.24 wt%), and have a wide range of MgO (4.29–16.67), CaO (3.58–8.50), and Na_2O (3.78–8.06 wt%) abundances. S^{2-} contents range from as low as 0.64 wt% to as high as 4.81 wt%. Additionally, although we did not intentionally include Cl^- in our starting composition, it was present in all runs. We suspect that one of our reagents (most likely FeS) may be contaminated with Cl^- . We have ruled out contamination from the NaCl pressure medium used in the PC experiments as the primary source of Cl^- because the MA experiments, which consist of a Cl^- -free ceramic octahedron as a pressure medium, also contain measurable amounts of Cl^- ([Table S3](#)). Although the Cl^- may have been present in variable amounts at the start of each experiment, it consistently partitioned entirely into the silicate melt (up to 2.44 wt%), and it was below detection in coexisting sulfide (detection limit 0.01 wt%) and metal (detection limit 0.01 wt%) phases. Micro-FTIR analyses of the glass in two experiments, with sample thicknesses < 170 μm , indicate ~ 1 to 6 ppm H_2O was present in these charges which are levels too low to significantly affect phase boundaries ([Médard and Grove, 2008](#)) or elemental partitioning ([Righter and Drake, 1999](#)).

The addition of Si metal to the bottom of each capsule, as well as higher concentrations of sulfur, led to the formation of numerous metals and sulfides in each experiment. EPMA analyses and stoichiometric compositions of each metal and sulfide phase are given in [Table S4](#). Pure Si metal is present within each experiment, indicating it was not completely consumed during the run. In some cases, the Si metal was veined with a Si–Cr metal mixture. The other metals in these experiments typically consisted of Si, Cr, and Fe with minor amounts of Ti and Mn. The sulfides were dominated by Fe and Cr as well as Ti and Mn. In a few cases, Ca- and Mg-bearing sulfides were present. These

results were used to calculate normative sulfides in [Table S1](#) before performing additional CIPW norm calculations on the sulfide-removed residual silicate compositions.

5.2. NAS_F phase equilibrium experiments

SiO_2 is present as a liquidus phase at all pressures investigated in this study for the NAS_F composition. At low pressures, orthopyroxene and SiO_2 are the liquidus phases. The orthopyroxene has an average composition of $\text{En}_{90}\text{Fs}_8\text{Wo}_2$ in all experiments up to 3 GPa ([Table 2](#) and [Table S2](#)). At approximately 3 GPa and 1800 $^\circ\text{C}$, garnet appears on the liquidus with orthopyroxene and SiO_2 . At pressures greater than 3 GPa, pyrope-rich garnet and SiO_2 are the liquidus phases. Clinopyroxene ($\text{En}_{66}\text{Fs}_9\text{Wo}_{25}$) becomes stable at higher pressures (≥ 2.5 GPa). As expected given the elevated SiO_2 abundances and lack of alkali elements, olivine is not stable at any pressure investigated with this composition (0.5–5 GPa).

EPMA analyses of each melt are provided in [Table S2](#). The melts consistently had high SiO_2 (54.62–59.55 wt%), low MnO (0.65–0.73 wt%), and low Cr_2O_3 (0.20–0.75 wt%). There was a wide range in TiO_2 (1.20–5.70), Al_2O_3 (4.44–17.29), FeO (4.95–9.22), MgO (8.60–15.18) and CaO (5.00–14.17) depending on the silicate phases present in a given run product. Although these experiments were run in molybdenum capsules, there was very little Mo^0 dissolved in the melt. The maximum MoO_2 abundance measured was 1.18 wt%, which most likely reflects a metal bleb that was close to the electron beam during analysis. Micro-FTIR analyses of glasses from four experimental charges from this study indicate an H_2O content typically much less than 0.1 wt% H_2O with one higher value of 0.3 wt%, which are levels too low to significantly affect phase boundaries ([Médard and Grove, 2008](#)) or elemental partitioning ([Righter and Drake, 1999](#)). Sample thicknesses varied from 48–175 μm .

6. DISCUSSION

6.1. Effect of alkalis on mercurian mineralogy

The mineralogy of Mercury's surface is currently unknown despite the collection of over 4.5 million UV–VIS spectra by the MESSENGER spacecraft ([Ernst et al., 2010; Holsclaw et al., 2010; Blewett et al., 2013; Izenberg et al., 2014](#)). Consequently, the mineralogy of the mercurian surface has typically been inferred (e.g., [Stockstill-Cahill et al., 2012; Charlier et al., 2013](#)) using chemical compositions of the surface determined by the XRS and GRS instruments onboard MESSENGER ([Nittler et al., 2011, 2013; Peplowski et al., 2011, 2012, 2014; Evans et al., 2012; Weider et al., 2012, 2015](#)). As stated previously, one of the most surprising results returned from MESSENGER was the elevated abundances of Na on the surface of the planet (global average of 3.5 wt% Na_2O), particularly at the high northern latitudes (average of 6.7 wt% Na_2O), that has been interpreted as being a geochemical feature of the lavas in the NVP ([Peplowski et al., 2014](#)). Consequently, we can compare and contrast the results of our high pressure phase equilib-

rium data for the two starting compositions (NAS_F and NAS_B), which have over a 5 wt% difference in Na₂O. Importantly, there are numerous differences between the two compositions we investigated as shown in Figs. 4, S3, and Table 1. In addition to an ~5 wt% difference in Na₂O abundance, there is also an ~5 wt% difference in FeO abundance that is related to the differences in oxygen fugacity, up to ~7 log₁₀ units, between the two sets of experiments (Tables 1 and 2). If the NAS_F experiments were run under the low oxygen fugacity conditions of the NAS_B experiments, it would have resulted in a net decrease in the amount of FeO in the NAS_F experiments, which would have caused a net increase in the silica activity by increasing the ratio of Si to other melt components in the NAS_F composition. This enhancement in silica activity in the NAS_F experiments would have caused even further displacement of the NAS_F composition from the olivine stability field.

The addition of alkali elements like Na to silicate melts results in a reduction of silica activity by reducing the number of Si–O–Si linkages in the melt, eventually leading to the stabilization of olivine over pyroxene (Mysen, 1987; Hirschmann et al., 1998; Charlier et al., 2013). Because our low pressure observation is that olivine is the liquidus phase in the NAS_B experiments and pyroxene is the liquidus phase for the NAS_F experiments, we contend that the mineralogical differences between the two compositions can be largely attributed to the differences in Na rather than the differences in oxygen fugacity between the NAS_F and NAS_B compositions. Furthermore, the NAS_F composition may not actually be representative of a mercurian composition, so we limited the number of experiments that were conducted to characterize the phase diagram for the NAS_F composition. Therefore, we present the experimental data for the experiments on the NAS_F composition, as is, without interpretation of the liquidus or mineral-in and mineral-out curves for lack of experimental constraints (Fig. S3). In order to construct these curves accurately, additional experiments are needed.

As expected, the addition of alkalis depresses the liquidus of the melt and displaces the stability field of SiO₂ to higher pressures. SiO₂ is a liquidus phase at 0.4 GPa in the NAS_F composition, but it does not hit the liquidus until pressures greater than 3.5 GPa when alkali elements are present (NAS_B). Furthermore, the appearance of SiO₂ on the high pressure liquidus of the NAS_B composition may be an artifact of O diffusion into our capsules, which reacts with Si metal to increase the SiO₂ content of our experiments. When alkali elements are present, pyroxene and SiO₂ are replaced on the liquidus at low pressures by forsteritic olivine. The stability field of pyroxene is also extended at high pressure in the NAS_B composition compared to the NAS_F composition by the destabilization of garnet. Importantly, this pyroxene composition can have up to 7 wt% Na₂O in its structure. Based on the mineralogical differences between the NAS_F and NAS_B compositions, we conclude that the expected mantle and surface mineralogy of Mercury will be strongly dependent on the abundances of alkali elements present.

Although we have not yet conducted 1-bar experiments, the results of our lowest pressure phase equilibrium

experiments can be combined with the CIPW norm calculations of the NVP composition from MESSENGER data (Table S1) as well as the experimental results from Charlier et al. (2013) to infer the surface mineralogy of Mercury. Charlier et al. (2013) conducted 1-bar crystallization experiments at elevated oxygen fugacity (at the fayalite–magnetite–quartz buffer) on two different mercurian surface compositions and showed orthopyroxene, plagioclase, as well as minor olivine, clinopyroxene, and tridymite should be present on the mercurian surface. The results from our lowest pressure phase equilibrium experiments indicate that olivine, low-calcium, low-iron pyroxene, as well as plagioclase are likely to be primary silicate minerals on the surface of Mercury. However, if there are regions on the surface with low Na₂O (i.e., NAS_F composition) and SiO₂ abundances similar to the NVP, we expect the disappearance of olivine and the appearance of SiO₂. We also expect the presence of Fe–Mn–Ti–Cr sulfides as the dominant sulfides on Mercury, with minor Mg- or Ca-sulfides. The results from our two experimental starting compositions and the two compositions examined by Charlier et al. (2013) yield similar mineralogical results for 3 distinct regions on Mercury. Therefore, one can expect similar mineralogy across the surface of the planet if the melt compositions have the same general characteristics as those already studied experimentally (i.e., low Fe, high Si, and high S). Crystallization experiments on these and similar compositions at 1-bar over a range of oxygen fugacities are needed in order to confirm this predicted mineralogy.

6.2. Models for the origin of the NVP lavas

Partial melts in the Earth's upper mantle are typically controlled by eutectic melting of olivine and pyroxene. The point (in *P–T* space) on a phase diagram of a primary melt composition that corresponds to multiple saturation on the liquidus with the minerals expected to have remained in the source after melting (i.e., olivine and pyroxene in Earth's upper mantle) is indicative of the average depth at which the melt separated from its source and rose to the surface (Asimow and Longhi, 2004). However, we do not have any insights into the expected mineralogy of the NVP source region, so we do not necessarily expect the *P–T* origin of the NVP lavas to correspond to one of the MSP's in the phase diagram (Fig. 4). In fact, the sheer volume of lava that was erupted supports the possibility of high degrees of partial melting, which might favor melting out all but the dominant mantle mineral phase.

Additional insights into the interpretation of the phase equilibrium data for the NAS_B composition could be determined based on the elevated abundance of Na in the NVP lavas. Na is an incompatible large-ion lithophile element, and so its distribution within Mercury's interior is predictable for a given set of hypothetical scenarios for the thermal and magmatic evolution of Mercury. The formation mechanism of Mercury is unknown at present, but there are two end-member possibilities that we consider for predicting the distribution of incompatible lithophile elements in Mercury's interior. If the silicate portion of Mercury never fully melted, Mercury's full inventory of

incompatible elements would be dispersed throughout its interior, probably in nearly chondritic abundances. This model for the evolution of Mercury's mantle and crust is analogous to studies that have used partial melting experiments of enstatite chondrite as an analogue for the melting of Mercury's interior (McCoy et al., 1999; Malavergne et al., 2010), where Mercury's mantle is assumed to have the composition of an enstatite chondrite. This model would be one way to explain the presence of alkalis at depth, which would support the possibility of the NVP forming from low degrees of partial melting deep within the mercurian mantle; however, we dismiss this model because it would require that Mercury's mantle is composed of undifferentiated enstatite chondrite material, which is not consistent with Mercury's highly differentiated state. Consequently, this scenario is not well supported in the literature, so we consider it only as an end-member where Na is present throughout Mercury's mantle (enstatite chondrites typically have ~5800 to 6900 ppm Na; Lodders and Fegley, 1998).

It is generally accepted that Mercury experienced some form of a magma ocean event (Brown and Elkins-Tanton, 2009; Riner et al., 2009; Charlier et al., 2013). A mercurian mantle that experienced a magma ocean would likely host much of its inventory of incompatible elements near the surface of the planet, similar to what is generally expected for the lunar magma ocean (Warren, 1985; de Vries et al., 2010; Elardo et al., 2011; Elkins-Tanton et al., 2011; Rapp and Draper, 2012). Unlike the Moon, however, the low FeO content of Mercury's mantle would have prohibited the formation of a floatation crust consisting of silicate minerals (Vander Kaaden and McCubbin, 2015). Therefore, the last minerals to form during a crystallizing mercurian magma ocean would be concentrated near the surface of the planet instead of at the base of a silicate primary crust as is the case for the Moon (Warren, 1985; de Vries et al., 2010; Elardo et al., 2011; Elkins-Tanton et al., 2011; Rapp and Draper, 2012). Furthermore, the low total FeO content of Mercury's mantle results in only minor density contrasts throughout the cumulate mantle (Vander Kaaden and McCubbin, 2015) and hence gravitational overturn of the mantle is unlikely to have occurred. Consequently, this inferred stratigraphy of incompatible elements concentrated towards the upper mantle/crust would be a permanent geochemical feature of a post magma ocean Mercury.

In the magma ocean scenario, the elevated abundance of Na in the NVP lavas is consistent with a shallow magmatic source region. Given that the first MSP in the NAS_B phase diagram is at 1.4 GPa, which corresponds to approximately one-quarter the depth of the mercurian mantle, we infer that the source for the NVP lavas had to be shallower than the first-observed MSP, and hence the low-pressure liquidus phase (olivine) was the only mineral left in the source during the partial melting event that produced the NVP lavas. This scenario is consistent with high degrees of partial melting (e.g., 15–30% melting for the Deccan Traps; Sen, 2001), which is potentially a common characteristic between flood volcanism on Mercury and flood volcanism on Earth (Hooper and Hawkesworth, 1993; Coffin and Eldholm,

1994; Fedorenko et al., 1996, 2000; Peate, 1997; Takahashi et al., 1998; Sen, 2001). In addition, a low pressure source region corresponds to the stability field of albitic plagioclase (Green and Hibberson, 1970), which could explain the elevated Na abundances even with high degrees of partial melting. The albitic plagioclase would have completely melted during partial melting to form the NVP lavas. The nepheline-normative characteristics of the NVP lavas, coupled with their elevated Cl[−] abundances (Evans et al., 2015), indicate that sodalite may have also been a minor phase in the NVP source region. The primary shortcoming of this model is the source of heat for melting the upper mantle of Mercury at about 4.0 Ga (Thomas et al., 2014), although other small terrestrial bodies in the Solar System have demonstrably circumnavigated this problem, as shown in the number of igneous lunar samples from approximately the same period of time and younger (Nyquist and Shih, 1992; Hiesinger et al., 2000, 2003; Elardo et al., 2014). This process could have been aided by a thermal boost from increased concentrations of incompatible lithophile heat-producing elements in the upper mantle, although they could have also been sequestered in a putative FeS layer (McCubbin et al., 2012; Smith et al., 2012).

Alternatively, the NVP lavas could have formed by low degrees of partial melting, which would likely require that at least two phases remained in the mantle source after partial melting. In this scenario, we look to the 1.4 GPa MSP between olivine and orthopyroxene as being the probable depth of origin. In this scenario, the elevated Na abundance of the NVP lavas is a consequence of low degrees of partial melting and the preferential incorporation of Na into the partial melt. The primary shortcoming of this model comes in producing such a large volume of magma from low degrees of partial melting deep within the mercurian interior; however we do not see any reason to exclude this scenario from contention.

We can rule out the other MSPs as the average depth of melting based on mineralogical considerations. In a scenario where the average depth of melting is 2.7 GPa, jadeite and orthopyroxene remain in the source region after partial melting. This scenario requires the presence of a large amount of Na deep within the mercurian interior to stabilize a major Na-bearing phase. This would require that Mercury has a highly non chondritic silicate composition with a preponderance of Na, regardless of whether Mercury experienced a magma ocean. This scenario is too unlikely to be seriously considered and would require too many unrealistic caveats to pursue further. Consequently, this MSP is not likely to have any petrogenetic meaning for the NVP lavas or the mercurian interior in general. Therefore, our results favor the origin of the NVP lavas by high degrees of partial melting of an olivine-dominant, pyroxene- and albitic plagioclase-bearing mantle source at low pressure.

If the source region for the northern volcanic plains lavas is in fact dominated by forsteritic olivine, it calls into question models for Mercury's bulk composition that have used CB and enstatite chondrite bulk compositions (e.g., Morgan and Anders, 1980; Taylor and Scott, 2004;

Brown and Elkins-Tanton, 2009; Malavergne et al., 2010), which indicate that Mercury's upper mantle is predominantly pyroxene as opposed to olivine. It is unclear to what extent the results from the present study can be applied to the bulk mineralogy of Mercury's upper mantle; however additional data are needed to constrain the bulk composition of Mercury, which is highly unconstrained at this time.

6.3. Partitioning of elements under highly reducing conditions

The reducing nature of Mercury has raised many questions regarding the geochemical behavior of lithophile elements in magmas at low oxygen fugacity on Mercury as well as other reducing bodies in the Solar System. In fact, interpretations of magmatic processes on Mercury are difficult at present because the number of experimental studies relevant to the extremely low fO_2 and high sulfur content of Mercury are very limited (McCoy et al., 1999; Malavergne et al., 2004, 2007; Liu et al., 2007; Rose-Weston et al., 2009; Ricolleau et al., 2011; Chabot et al., 2014, 2015; Wykes et al., 2015). At such reducing conditions, elements are likely to deviate from their typical geochemical behavior displayed at higher oxygen fugacity (e.g., McCoy et al., 1999; Foley et al., 2005; McCubbin et al., 2012). For example, lithophile elements such as Mg and Ca display chalcophile behavior in some highly reduced chondrites and achondrites forming the minerals oldhamite [(Ca,Mg,Fe)₂S] and niningerite [(Mg,Fe,Mn)S] (McCoy et al., 1999). Other than the highly reduced enstatite chondrites and achondrites, we do not have many natural examples of what to expect with respect to element behavior in such oxygen-starved systems. Fortunately, a number of experimental studies have reported on the distributions of elements among various phases at a range of oxygen fugacities, so it is possible to make some predictions about how, and under what conditions, certain elements would lose their lithophile behavior. Rose-Weston et al. (2009) looked at the effect of pressure, temperature, and oxygen fugacity on metal–silicate partitioning of numerous

elements, including S, and observed that S becomes more siderophile with increasing P and less siderophile with increasing T . More recently, Chabot et al., (2014, 2015)) have examined partitioning behavior in the Fe–S and Fe–S–O system. These studies, conducted between 1 atm and 9 GPa over the temperature range 1050–1600 °C, lead to three main conclusions: (1) pressure affects solid metal/liquid metal partitioning, (2) most elements show O-avoidance similar to their S-avoidance tendencies, and (3) none of the experiments were able to match the MESSENGER results for the Fe and S on Mercury's surface. Each of these studies has advanced our understanding of sulfur solubility and elemental partitioning during planetary differentiation; however, they have not explored highly reducing, sulfur bearing conditions that are as extreme as those observed on Mercury.

Experiments run using the NAS_B composition resulted in silicate, metal, and sulfide phases (Table 2). Although there is a wide range in P – T – fO_2 space of the experimental charges, we have calculated metal–silicate and sulfide–silicate partition coefficients for each charge, when applicable, using Eq. (3) below:

$$D^{A-B} = \frac{X_A}{X_B} \quad (3)$$

where X_A is the mole fraction of element X in phase A (metal or sulfide) and X_B is the mole fraction of element X in phase B (silicate). Fig. 5 shows the average D values for each element in our experimental charges. The D values for Cl were calculated using the detection limit of Cl in our metals and sulfides, therefore providing an upper limit estimate for D_{Cl} . The error bars of each element represent the minimum and maximum D values across all of our NAS_B experiments. The geochemical affinity of a particular element is determined by the quadrant in which the average D value plots in Fig. 5.

Our results indicate Al, Na, K, Mg, Ca, and Cl remain lithophile at all pressures and temperatures we investigated. However, Ca, Mg, and Na display limited chalcophile

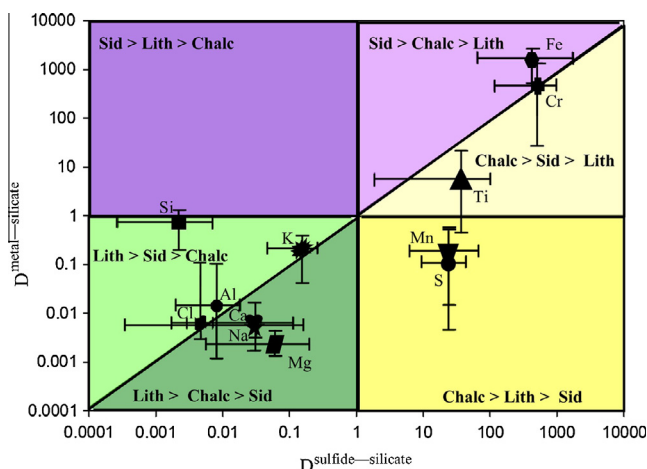


Fig. 5. Elemental partitioning of elements from NAS_B experiments. The symbol for each element is the average D value from all of the experiments in Tables S3–S4. The error bars represent the maximum and minimum D values from all experimental charges. The D values for Cl were calculated using the EPMA detection limits in the metals and sulfides. The affinity of an element is depicted by which region of the graph it falls in. Sid: Siderophile, Lith: Lithophile, Chalc: Chalcophile.

behavior over that of siderophile. Si does not display any evidence of chalcophile behavior, but it is both lithophile and siderophile. S remains chalcophile but also displays lithophile behavior at these conditions that out-competes its siderophile character. Ti, Mn, and Cr display chalcophile behavior at the fO_2 conditions we investigated. Ti and Cr are more siderophile than lithophile but Mn is more lithophile than siderophile. Our results also indicate that Fe loses its lithophile character at the conditions we investigated, and it is more siderophile than chalcophile. MESSENGER XRS data indicates a positive correlation between S and Ca abundances on the mercurian surface, leading to inferences that oldhamite is the dominant sulfide phase (Weider et al., 2014). Based on our experimental results, Ca and Mg would not be substantial components in sulfides on Mercury unless the abundance of Fe, Cr, Mn, and Ti were insufficient relative to available sulfide components in the system.

7. CONCLUSION

The surface of Mercury lacks spectral absorption features that can be used to definitively determine surface mineralogy by UV–VIS spectroscopy; however, our phase equilibrium results, previous mercurian phase equilibrium results (Charlier et al., 2013), as well as CIPW norm calculations can be used to infer the mineralogy of Mercury's surface. The surface is likely dominated by forsteritic olivine, enstatitic pyroxene, and plagioclase. For regions of the surface with lower sodium and elevated SiO_2 , orthopyroxene, plagioclase, and quartz or tridymite can be expected as stable surface minerals. Under the highly reducing conditions of Mercury, typically lithophile elements like Cr, Mn, and Ti become chalcophile and partition into sulfide phases. Consequently, Fe-, Cr-, Mn-, and Ti-bearing sulfides can be expected on the surface of Mercury with possible Mg- and Ca-bearing sulfides if Fe, Cr, Mn, and Ti are not present to bond with S^{2-} .

Partial melting of the mercurian interior resulted in flood volcanism that produced lavas with a bulk composition similar to terrestrial boninites, with notably higher abundances of alkalis. On Earth, boninites typically form in oxidized arc environments associated with subduction zones (Hickey and Frey, 1982; Cameron et al., 1983; Sobolev and Danyushevsky, 1994; Polat et al., 2002), but this is certainly not the case for the origin of mercurian boninites. Instead, our phase equilibrium results indicate they formed through partial melting of the shallow mercurian interior from a source region that consisted primarily of forsteritic olivine, orthopyroxene, and albitic plagioclase. Such a phase assemblage does not require the aid of water or oxidizing conditions to form boninitic melt compositions. Consequently, a new and novel boninite-formation mechanism within the Solar System may operate on Mercury. Furthermore, this process would represent a previously unrecognized mechanism for producing SiO_2 -rich, secondary crustal materials on a planet without the aid of water or plate tectonics. The results from this study further support Mercury as an endmember among the rocky planets in the Solar System.

ACKNOWLEDGEMENTS

Data reported in this paper including EPMA analyses of experimental charges are available in the [Supporting Materials](#). The authors would like to thank Whitney McCutcheon for assisting in FTIR analyses and Alison Santos for helpful discussions and assisting in Multi-Anvil runs. We also thank the MESSENGER Science Team, with special thanks to the MESSENGER Geochemistry Discipline Group, for fruitful discussions regarding the interpretation of MESSENGER data. The authors also thank Rachel Klima for providing an estimate for the number of UV–VIS spectra collected by the MESSENGER spacecraft. We are appreciative of comments from Michael Toplis (A.E.), as well as reviewers Nancy Chabot, Karen Stockstill-Cahill, and an anonymous reviewer which helped to improve this manuscript. This work was funded by a NASA Cosmochemistry Grant NNX14AK43G to F.M.M. This work was also supported by a New Mexico Space Grant Consortium Fellowship and by NASA Headquarters under the NASA Earth and Space Science Fellowship Program-Grant NNX15AQ80H both awarded to K.E.V.K.

APPENDIX A. SUPPLEMENTARY DATA

Supplementary data associated with this article can be found, in the online version, at <http://dx.doi.org/10.1016/j.gca.2015.10.016>.

REFERENCES

- Agee C. B., Li J., Shannon M. C. and Circone S. (1995) Pressure–temperature phase diagram for the Allende meteorite. *J. Geophys. Res. Solid Earth* **100**, 17725–17740.
- Ardia P., Hirschmann M. M., Withers A. C. and Stanley B. D. (2013) Solubility of CH_4 in a synthetic basaltic melt, with applications to atmosphere-magma ocean-core partitioning of volatiles and to the evolution of the Martian atmosphere. *Geochim. Cosmochim. Acta* **114**, 52–71.
- Asimow P. D. and Longhi J. (2004) The significance of multiple saturation points in the context of polybaric near-fractional melting. *J. Petrol.* **45**, 2349–2367.
- Beattie P. (1993) Olivine-melt and orthopyroxene-melt equilibria. *Contrib. Miner. Petrol.* **115**, 103–111.
- Beermann O., Botcharnikov R. E., Holtz F., Diedrich O. and Nowak M. (2011) Temperature dependence of sulfide and sulfate solubility in olivine-saturated basaltic magmas. *Geochim. Cosmochim. Acta* **75**, 7612–7631.
- Berger J. A. (2012) *Effect of halite and calcite coatings on thermal infrared spectra with implications for Mars exploration* M. S. thesis. University of New Mexico.
- Berthet S., Malavergne V. and Righter K. (2009) Melting of the Indarch meteorite (EH4 chondrite) at 1 GPa and variable oxygen fugacity: implications for early planetary differentiation processes. *Geochim. Cosmochim. Acta* **73**, 6402–6420.
- Blewett D. T., Vaughan W. M., Xiao Z., Chabot N. L., Denevi B. W., Ernst C. M., Helbert J., D'Amore M., Maturilli A., Head J. W. and Solomon S. C. (2013) Mercury's hollows: constraints on formation and composition from analysis of geological setting and spectral reflectance. *J. Geophys. Res. Planets* **118**, 1013–1032.
- Brown S. M. and Elkins-Tanton L. T. (2009) Compositions of Mercury's earliest crust from magma ocean models. *Earth Planet. Sci. Lett.* **286**, 446–455.

- Burkemper L. K., Agee C. B. and Garcia K. A. (2012) Constraints on core formation from molybdenum solubility in silicate melts at high pressure. *Earth Planet. Sci. Lett.* **335**–**336**, 95–104.
- Byrne P. K., Klimczak C., Sengor A. M. C., Solomon S. C., Watters T. R. and Hauck, II, S. A. (2014) Mercury's global contraction much greater than earlier estimates. *Nat. Geosci.* **7**, 301–307.
- Cameron W. E., McCulloch M. T. and Walker D. A. (1983) Boninite petrogenesis: chemical and Nd–Sr isotopic constraints. *Earth Planet. Sci. Lett.* **65**, 75–89.
- Campbell I. H. and Taylor S. R. (1983) No water, no granites, no oceans, no continents. *Geophys. Res. Lett.* **10**, 1061–1064.
- Carmichael I. S. E., Nicholls J. and Smith A. L. (1970) Silica activity in igneous rocks. *Am. Mineral.* **55**, 246–263.
- Chabot N. L., Wollack E. A., Klima R. L. and Minitti M. E. (2014) Experimental constraints on Mercury's core composition. *Earth Planet. Sci. Lett.* **390**, 199–208.
- Chabot N. L., Wollack E. A. and Humayun M. (2015) The effect of oxygen as a light element in metallic liquids on partitioning behavior. *Meteorit. Planet. Sci.* **50**(4), 530–546.
- Charlier B., Grove T. L. and Zuber M. T. (2013) Phase equilibria of ultramafic compositions on Mercury and the origin of the compositional dichotomy. *Earth Planet. Sci. Lett.* **363**, 50–60.
- Coffin M. F. and Eldholm O. (1994) Large igneous provinces: crustal structure, dimensions, and external consequences. *Rev. Geophys.* **32**, 1–36.
- Cross W., Iddings J. P., Pirsson L. V. and Washington H. S. (1903) *Quantitative Classification of Igneous Rocks*. University of Chicago Press.
- Day J. M. D., Ash R. D., Liu Y., Bellucci J. J., Rumble, III, D., McDonough W. F., Walker R. J. and Taylor L. A. (2009) Early formation of evolved asteroidal crust. *Nature* **457**, 179–182.
- de Vries J., van den Berg A. and van Westrenen W. (2010) Formation and evolution of a lunar core from ilmenite-rich magma ocean cumulates. *Earth Planet. Sci. Lett.* **292**, 139–147.
- Denevi B. W., Ernst C. M., Meyer H. M., Robinson M. S., Murchie S. L., Whitten J. L., Head J. W., Watters T. R., Solomon S. C., Ostrach L. R., Chapman C. R., Byrne P. K., Klimczak C. and Peplowski P. N. (2013) The distribution and origin of smooth plains on Mercury. *J. Geophys. Res. Planets* **118**, 891–907.
- Dixon J. E., Stolper E. M. and Holloway J. R. (1995) An experimental study of water and carbon dioxide solubilities in mid ocean ridge basaltic liquids. I. Calibration and solubility models. *J. Petrol.* **36**, 1607–1631.
- Elardo S. M., Draper D. S. and Shearer C. K. (2011) Lunar magma ocean crystallization revisited: bulk composition, early cumulate mineralogy, and the source regions of the highlands Mg-suite. *Geochim. Cosmochim. Acta* **75**, 3024–3045.
- Elardo S. M., Shearer C. K., Fagan A. L., Borg L. W., Gaffney A. M., Burger P. V., Neal C. R., Fernandes V. A. and McCubbin F. M. (2014) The origin of young mare basalts inferred from lunar meteorites Northwest Africa 4734, 032, and LaPaz Icefield 02205. *Meteorit. Planet. Sci.* **49**, 261–291.
- Elkins-Tanton L. T., Burgess S. and Yin Q. Z. (2011) The lunar magma ocean: reconciling the solidification process with lunar petrology and geochronology. *Earth Planet. Sci. Lett.* **304**, 326–336.
- Ernst C. M., Murchie S. L., Barnouin-Jha O. S., Robinson M. S., Denevi B. W., Blewett D. T., Head J. W., Izenberg N. R. and Solomon S. C. (2010) Exposure of spectrally distinct material by impact craters on Mercury: implications for global stratigraphy. *Icarus* **209**, 210–223.
- Evans L. G., Peplowski P. N., Rhodes E. A., Lawrence D. J., McCoy T. J., Nittler L. R., Solomon S. C., Sprague A. L., Stockstill-Cahill K. R., Starr R. D., Weider S. Z., Boynton W. V., Hamara D. K. and Goldsten J. O. (2012) Major-element abundances on the surface of Mercury: results from the MESSENGER Gamma-Ray spectrometer. *J. Geophys. Res. Planets* **117**, E00L07.
- Evans L. G., Peplowski P. N., Killen R. M., Potter A. E. and Sprague A. L. (2013) Variable sodium on the surface of mercury: implications for surface chemistry and the exosphere. *44th Lunar Planet. Sci. Conf.* The Woodlands, TX, #2033.
- Evans L. G., Peplowski P. N., McCubbin F. M., McCoy T. J., Nittler L. R., Zolotov M. Y., Ebel D. S., Lawrence D. J., Starr R. D., Weider S. Z. and Solomon S. C. (2015) Chlorine on the surface of Mercury: MESSENGER Gamma-ray measurements and implications for the planet's formation and evolution. *Icarus* **257**, 417–427.
- Fedorenko V., Lightfoot P. C., Czamanske G. K., Hawkesworth C. J., Wooden J. L. and Ebel D. S. (1996) Petrogenesis of the Siberian flood-basalt sequence at Noril'sk. *Int. Geol. Rev.* **38**, 99–135.
- Fedorenko V., Czamanske G., Zen'ko T., Budahn J. and Siems D. (2000) Field and geochemical studies of the melilite-bearing Arydzhangsky suite, and an overall perspective on the Siberian alkaline-ultramafic flood-volcanic rocks. *Int. Geol. Rev.* **42**, 769–804.
- Foley C. N., Wadhwa M., Borg L. E., Janney P. E., Hines R. and Grove T. L. (2005) The early differentiation history of Mars from W-182-Nd-142 isotope systematics in the SNC meteorites. *Geochim. Cosmochim. Acta* **69**, 4557–4571.
- Green D. H. and Hibberson W. (1970) The instability of plagioclase in peridotite at high pressure. *Lithos* **3**, 209–221.
- Hauck, II, S. A., Margot J. L., Solomon S. C., Phillips R. J., Johnson C. L., Lemoine F. G., Mazarico E., McCoy T. J., Padovan S., Peale S. J., Perry M. E., Smith D. E. and Zuber M. T. (2013) The curious case of Mercury's internal structure. *J. Geophys. Res. Planets* **118**, 1204–1220.
- Head J. W., Chapman C. R., Strom R. G., Fassett C. I., Denevi B. W., Blewett D. T., Ernst C. M., Watters T. R., Solomon S. C., Murchie S. L., Prockter L. M., Chabot N. L., Gillis-Davis J. J., Whitten J. L., Goudge T. A., Baker D. M. H., Hurwitz D. M., Ostrach L. R., Xiao Z., Merline W. J., Kerber L., Dickson J. L., Oberst J., Byrne P. K., Klimczak C. and Nittler L. R. (2011) Flood volcanism in the northern high latitudes of Mercury revealed by MESSENGER. *Science* **333**, 1853–1856.
- Hickey R. L. and Frey F. A. (1982) Geochemical characteristics of boninite series volcanics: implications for their source. *Geochim. Cosmochim. Acta* **46**, 2099–2115.
- Hiesinger H., Jaumann R., Neukum G. and Head J. W. (2000) Ages of mare basalts on the lunar nearside. *J. Geophys. Res. Planets* **105**, 29239–29275.
- Hiesinger H., Head J. W., Wolf U., Jaumann R. and Neukum G. (2003) Ages and stratigraphy of mare basalts in Oceanus Procellarum, Mare Nubium, Mare Cognitum, and Mare Insularum. *J. Geophys. Res. Planets*, 108.
- Hirschmann M. M., Baker M. B. and Stolper E. M. (1998) The effect of alkalis on the silica content of mantle-derived melts. *Geochim. Cosmochim. Acta* **62**, 883–902.
- Holsclaw G. M., McClintock W. E., Robinson M. S., Domingue D. L., Izenberg N. R., Blewett D. T. and Sprague A. L. (2010) A comparison of ultraviolet to near-infrared spectral properties of Mercury and the Moon as observed by MESSENGER. *Icarus* **209**, 179–194.
- Holzheid A. and Grove T. L. (2002) Sulfur saturation limits in silicate melts and their implications for core formation scenarios for terrestrial planets. *Am. Mineral.* **87**, 227–237.
- Hooper P. R. and Hawkesworth C. J. (1993) Isotopic and geochemical constraints on the origin and evolution of the Columbia River basalt. *J. Petrol.* **34**, 1203–1246.

- Irvine T. N. and Baragar W. R. A. (1971) A guide to the chemical classification of the common volcanic rocks. *Can. J. Earth Sci.* **8** (5), 523–548.
- Izenberg N. R., Klima R. L., Murchie S. L., Blewett D. T., Holsclaw G. M., McClintock W. E., Malaret E., Mauceri C., Vilas F., Sprague A. L., Helbert J., Domingue D. L., Head J. W., Goudge T. A., Solomon S. C., Hibbitts C. A. and Dyar M. D. (2014) The low-iron, reduced surface of Mercury as seen in spectral reflectance by MESSENGER. *Icarus* **228**, 364–374.
- Jolliff B. L. (1991) Fragments of quartz monzodiorite and felsite in Apollo 14 soil particles. *Proc. Lunar Planet. Sci.* **21**, 101–118.
- Jolliff B. L., Floss C., McCallum I. S. and Schwartz J. M. (1999) Geochemistry, petrology, and cooling history of 14161,7373: a plutonic lunar sample with textural evidence of granitic-fraction separation by silicate-liquid immiscibility. *Am. Mineral.* **84**, 821–837.
- Krawczynski M. J. and Grove T. L. (2012) Experimental investigation of the influence of oxygen fugacity on the source depths for high titanium lunar ultramafic magmas. *Geochim. Cosmochim. Acta* **79**, 1–19.
- Le Bas M. J. (2000) IUGS reclassification of the high-Mg and picritic volcanic rocks. *J. Petrol.* **41**, 1467–1470.
- Le Bas M. J. and Streckeisen A. L. (1991) The IUGS systematics of igneous rocks. *J. Geol. Soc., Lond.* **148**, 825–833.
- Le Maitre R. W. (1984) A proposal by the IUGS Subcommittee on the Systematics of Igneous Rocks for a chemical classification of volcanic rocks based on the total alkali silica (TAS) diagram. *Aust. J. Earth Sci.* **31**, 243–255.
- Le Maitre R. W., Streckeisen A., Zanettin B., Le Bas M. J., Bonin B., Bateman P., Bellieni G., Dudek A., Efremova S., Keller J., Lameyre J., Sabine P. A., Schmid R., Sorensen H. and Woolley A. R. (2002) *Igneous Rocks: A Classification and Glossary of Terms*. Cambridge University Press, New York, 236 pages.
- Liu Y., Samaha N.-T. and Baker D. R. (2007) Sulfur concentration at sulfide saturation (SCSS) in magmatic silicate melts. *Geochim. Cosmochim. Acta* **71**, 1783–1799.
- Lodders K. and Fegley, Jr., B. (1998) *The Planetary Scientist's Companion*. Oxford University Press, 400 pages, ISBN-13:978-0195116946.
- Malavergne V., Siebert J., Guyot F., Gautron L., Combes R., Hammouda T., Borensztajn S., Frost D. and Martinez I. (2004) Si in the core? New high-pressure and high-temperature experimental data. *Geochim. Cosmochim. Acta* **68**, 4201–4211.
- Malavergne V., Berthet S. and Righter K. (2007) Formation of CaS–MgS in enstatite chondrites and achondrites as a function of redox conditions and temperature: constraints on their evolution in a planetesimal and in a proto-planet. *38th Lunar Planet. Sci. Conf. Lunar Planet. Inst., Houston, TX. #1737* (abstr.).
- Malavergne V., Toplis M. J., Berthet S. and Jones J. (2010) Highly reducing conditions during core formation on Mercury: implications for internal structure and the origin of a magnetic field. *Icarus* **206**, 199–209.
- Malavergne V., Cordier P., Righter K., Brunet F., Zanda B., Adda A., Smith T., Bureau H., Surlé S., Raepsaet C., Charon E. and Hewins R. H. (2014) How Mercury can be the most reduced terrestrial planet and still store iron in its mantle. *Earth Planet. Sci. Lett.* **394**, 186–197.
- Mandeville C. W., Webster J. D., Rutherford M. J., Taylor B. E., Timbal A. and Faure K. (2002) Determination of molar absorptivities for infrared absorption bands of H₂O in andesitic glasses. *Am. Mineral.* **87**, 813–821.
- Mavrogenes J. A. and O'Neill H. S. C. (1999) The relative effects of pressure, temperature and oxygen fugacity on the solubility of sulfide in mafic magmas. *Geochim. Cosmochim. Acta* **63**, 1173–1180.
- McCoy T. J., Dickinson T. L. and Lofgren G. E. (1999) Partial melting of the Indarch (EH4) meteorite: a textural, chemical, and phase relations view of melting and melt migration. *Meteorit. Planet. Sci.* **34**, 735–746.
- McCubbin F. M., Riner M. A., Vander Kaaden K. E. and Burkemper L. K. (2012) Is Mercury a volatile-rich planet? *Geophys. Res. Lett.*, 39.
- McCubbin F. M., Vander Kaaden K. E., Tartese R., Boyce J. W., Mikhail S., Whitson E. S., Bell A. S., Anand M., Franchi I. A., Wang J. and Hauri E. H. (2015) Experimental investigation of F, Cl, and OH partitioning between apatite and Fe-rich basaltic melt at 1.0–1.2 GPa and 950–1000 °C. *Am. Mineral.* **100**, 1790–1802.
- Médard E. and Grove T. L. (2008) The effect of H₂O on the olivine liquidus of basaltic melts: experiments and thermodynamic models. *Contrib. Miner. Petrol.* **155**, 417–432.
- Morgan J. W. and Anders E. (1980) Chemical composition of Earth, Venus, and Mercury. *Proc. Natl. Acad. Sci. U.S.A.* **77**, 6973–6977.
- Moune S., Holtz F. and Botcharnikov R. E. (2009) Sulphur solubility in andesitic to basaltic melts: implications for Hekla volcano. *Contrib. Miner. Petrol.* **157**, 691–707.
- Murchie S. L., Klima R. L., Denevi B. W., Ernst C. M., Keller M. R., Domingue D. L., Blewett D. T., Chabot N. L., Hash C., Malaret E., Izenberg N. R., Vilas F., Nittler L. R. and Head J. W. (2015) Orbital multispectral mapping of Mercury using the MESSENGER Mercury Dual Imaging System: evidence for the origins of plains units and low-reflectance material. *Icarus*.
- Murthy V. M., van Westrenen W. and Fei Y. W. (2003) Experimental evidence that potassium is a substantial radioactive heat source in planetary cores. *Nature* **423**, 163–165.
- Mysen B. O. (1987) Magmatic silicate melts: relations between bulk composition, structure, and properties. In *Magmatic Properties: Physicochemical Principles* (ed. B. O. Mysen). Geochemical Society, University Park, PA, pp. 375–400.
- Nittler L. R., Starr R. D., Weider S. Z., McCoy T. J., Boynton W. V., Ebel D. S., Ernst C. M., Evans L. G., Goldsten J. O., Hamara D. K., Lawrence D. J., McNutt R. L., Schlemm C. E., Solomon S. C. and Sprague A. L. (2011) The major-element composition of Mercury's surface from MESSENGER X-ray spectrometry. *Science* **333**, 1847–1850.
- Nittler L., Weider S. and Solomon S. C. (2013) The composition of Mercury's crust from MESSENGER observations. *Mineral. Mag.* **77**, 1856.
- Nyquist L. E. and Shih C. Y. (1992) The isotopic record of lunar volcanism. *Geochim. Cosmochim. Acta* **56**, 2213–2234.
- O'Neill H. S. C. (1986) Mo–MoO₂ (MOM) oxygen buffer and the free energy of formation of MoO₂. *Am. Mineral.* **71**, 1007–1010.
- O'Neill H. S. C. and Eggins S. M. (2002) The effect of melt composition on trace element partitioning: an experimental investigation of the activity coefficients of FeO, NiO, CoO, MoO₂ and MoO₃ in silicate melts. *Chem. Geol.* **186**, 151–181.
- Ostrach L. R., Robinson M. S., Whitten J. L., Fassett C. I., Strom R. G., Head J. W. and Solomon S. C. (2015) Extent, age, and resurfacing history of the northern smooth plains on Mercury from MESSENGER observations. *Icarus* **250**, 602–622.
- Papike J. J., Karner J. M. and Shearer C. K. (2005) Comparative planetary mineralogy: valence state partitioning of Cr, Fe, Ti, and V among crystallographic sites in olivine, pyroxene, and spinel from planetary basalts. *Am. Mineral.* **90**, 277–290.
- Peate D. W. (1997) The Parana-Etendeka Province. In *Large Igneous Provinces: Continental, Oceanic, and Planetary Flood Volcanism*. The American Geophysical Union, pp. 217–245.
- Peplowski P. N., Evans L. G., Hauck S. A., McCoy T. J., Boynton W. V., Gillis-Davis J. J., Ebel D. S., Goldsten J. O., Hamara D. K., Lawrence D. J., McNutt R. L., Nittler L. R., Solomon S.

- C., Rhodes E. A., Sprague A. L., Starr R. D. and Stockstill-Cahill K. R. (2011) Radioactive elements on Mercury's surface from MESSENGER: implications for the planet's formation and evolution. *Science* **333**, 1850–1852.
- Peplowski P. N., Lawrence D. J., Rhodes E. A., Sprague A. L., McCoy T. J., Denevi B. W., Evans L. G., Head J. W., Nittler L. R., Solomon S. C., Stockstill-Cahill K. R. and Weider S. Z. (2012) Variations in the abundances of potassium and thorium on the surface of Mercury: results from the MESSENGER Gamma-Ray spectrometer. *J. Geophys. Res. Planets* **117**, E00L04.
- Peplowski P. N., Evans L. G., Stockstill-Cahill K. R., Lawrence D. J., Goldsten J. O., McCoy T. J., Nittler L. R., Solomon S. C., Sprague A. L., Starr R. D. and Weider S. Z. (2014) Enhanced sodium abundance in Mercury's north polar region revealed by the MESSENGER Gamma-Ray spectrometer. *Icarus* **228**, 86–95.
- Peplowski P. N., Lawrence D. J., Evans L. G., Klima R. L., Blewett D. T., Goldsten J. O., Murchie S. L., McCoy T. J., Nittler L. R., Solomon S. C., Starr R. D. and Weider S. Z. (2015) Constraints on the abundance of carbon in near-surface materials on Mercury: results from the MESSENGER Gamma-Ray spectrometer. *Planet. Space Sci.* **108**, 98–107.
- Polat A., Hofmann A. W. and Rosing M. T. (2002) Boninite-like volcanic rocks in the 3.7–3.8 Ga Isua greenstone belt, West Greenland: geochemical evidence for intra-oceanic subduction zone processes in the early Earth. *Chem. Geol.* **184**(3–4), 231–254.
- Rapp J. F. and Draper D. S. (2012) Experimental fractional crystallization of the lunar magma ocean. *Lunar Planet. Sci. Conf. XLIII*. Lunar Planet. Inst., Woodlands, TX, p. 2048.
- Ricolleau A., Fei Y., Corgne A., Siebert J. and Badro J. (2011) Oxygen and silicon contents of Earth's core from high pressure metal-silicate partitioning experiments. *Earth Planet. Sci. Lett.* **310**, 409–421.
- Righter K. and Drake M. J. (1999) Effect of water on metal-silicate partitioning of siderophile elements: a high pressure and temperature terrestrial magma ocean and core formation. *Earth Planet. Sci. Lett.* **171**, 383–399.
- Riner M. A., Lucey P. G., Desch S. J. and McCubbin F. M. (2009) Nature of opaque components on Mercury: insights into a Mercurian magma ocean. *Geophys. Res. Lett.* **36**(2).
- Riner M. A., McCubbin F. M., Lucey P. G., Taylor G. J. and Gillis-Davis J. J. (2010) Mercury surface composition: integrating petrologic modeling and remote sensing data to place constraints on FeO abundance. *Icarus* **209**, 301–313.
- Rose-Weston L., Brenan J. M., Fei Y. W., Secco R. A. and Frost D. J. (2009) Effect of pressure, temperature, and oxygen fugacity on the metal-silicate partitioning of Te, Se, and S: Implications for earth differentiation. *Geochim. Cosmochim. Acta* **73**, 4598–4615.
- Santos A. R., Agee C. B., McCubbin F. M., Shearer, Jr., C. K., Burger P. V., Tartèse R. and Anand M. (2015) Petrology of igneous clasts in Northwest Africa 7034: implications for the petrologic diversity of the Martian crust. *Geochim. Cosmochim. Acta* **157**, 56–85.
- Sautter V., Toplis M. J., Wiens R. C., Cousin A., Fabre C., Gasnault O., Maurice S., Forni O., Lasue J., Ollila A., Bridges J. C., Mangold N., Le Mouéléc S., Fisk M., Meslin P. Y., Beck P., Pinet P., Le Déit L., Rapin W., Stolper E. M., Newsom H., Dyar D., Lanza N., Vaniman D., Clegg S. and Wray J. J. (2015) In situ evidence for continental crust on early Mars. *Nat. Geosci.* **8**, 605–609.
- Seddio S. M., Jolliff B. L., Korotev R. L. and Zeigler R. A. (2013) Petrology and geochemistry of lunar granite 12032,366-19 and implications for lunar granite petrogenesis. *Am. Mineral.* **98**, 1697–1713.
- Sehlke A. and Whittington A. G. (2015) Rheology of lava flows on Mercury: an analog experimental study. *JGR: Planets*. <http://dx.doi.org/10.1002/2015JE004792>.
- Sen G. (2001) Generation of Deccan trap magmas. *Proc. Indian Acad. Sci. (Earth Planet. Sci.)* **110**, 409–431.
- Sharp Z. D., McCubbin F. M. and Shearer, Jr., C. K. (2013) A hydrogen-based oxidation mechanism relevant to planetary formation. *Earth Planet. Sci. Lett.* **380**, 88–97.
- Siebert J., Malavergne V., Guyot F., Combes R. and Martinez I. (2004) The behaviour of sulphur in metal-silicate core segregation experiments under reducing conditions. *Phys. Earth Planet. Inter.* **143–144**, 433–443.
- Smith D. E., Zuber M. T., Phillips R. J., Solomon S. C., Hauck S. A., Lemoine F. G., Mazarico E., Neumann G. A., Peale S. J., Margot J., Johnson C. L., Torrence M. H., Perry M. E., Rowlands D. D., Goossens S., Head J. W. and Taylor A. H. (2012) Gravity field and internal structure of Mercury from MESSENGER. *Science*.
- Sobolev A. V. and Danyushevsky L. V. (1994) Petrology and geochemistry of boninites from the north termination of the Tonga Trench: constraints on the generation conditions of primary high-Ca boninite magmas. *J. Petrol.* **35**, 1183–1211.
- Stockstill-Cahill K. R., McCoy T. J., Nittler L. R., Weider S. Z. and Hauck, III, S. A. (2012) Magnesium-rich crustal compositions on Mercury: implications for magmatism from petrologic modeling. *J. Geophys. Res.* **117**, E00L15.
- Stolper E. M., Baker M. B., Newcombe M. E., Schmidt M. E., Treiman A. H., Cousin A., Dyar M. D., Fisk M. R., Gellert R., King P. L., Leshin L., Maurice S., McLennan S. M., Minitti M. E., Perrett G., Rowland S., Sautter V., Wiens R. C. and Team M. S. L. S. (2013) The petrochemistry of Jake_M: a Martian Mugearite. *Science* **341**.
- Takahashi E., Nakajima K. and Wright T. L. (1998) Origin of the Columbia River basalts: melting model of a heterogeneous plume head. *Earth Planet. Sci. Lett.* **162**, 63–80.
- Tauster S. J., Pecoraro T. A. and Chianelli R. R. (1980) Structure and properties of molybdenum sulfide: correlation of O₂ chemisorption with hydrosulfurization activity. *J. Catal.* **63**, 515–519.
- Taylor G. J. and Scott E. R. D. (2004) Mercury. In *Treatise on Geochemistry: Meteorites, Comets, and Planets* (ed. A. M. Davis). Elsevier, Amsterdam, The Netherlands, pp. 477–485.
- Thomas R. J., Rothery D. A., Conway S. J. and Anand M. (2014) Long-lived explosive volcanism on Mercury. *Geophys. Res. Lett.* **41**, 6084–6092.
- Vander Kaaden K. E. and McCubbin F. M. (2015) Exotic crust formation on Mercury: consequences of a shallow, FeO-poor mantle. *J. Geophys. Res. Planets* **120**, 195–209.
- Vander Kaaden K. E., Agee C. B. and McCubbin F. M. (2015) Density and compressibility of the molten lunar picritic glasses: implications for the roles of Ti and Fe in the structures of silicate melts. *Geochim. Cosmochim. Acta* **149**, 1–20.
- Wade J. and Wood B. J. (2005) Core formation and the oxidation state of the Earth. *Earth Planet. Sci. Lett.* **236**, 78–95.
- Warren P. H. (1985) The magma ocean concept and lunar evolution. *Annu. Rev. Earth Planet. Sci.* **13**, 201–240.
- Weider S. Z., Nittler L. R., Starr R. D., McCoy T. J., Stockstill-Cahill K. R., Byrne P. K., Denevi B. W., Head J. W. and Solomon S. C. (2012) Chemical heterogeneity on Mercury's surface revealed by the MESSENGER X-Ray Spectrometer. *J. Geophys. Res. Planets* **117**.
- Weider S. Z., Nittler L. R., Starr R. D., McCoy T. J. and Solomon S. C. (2014) Variations in the abundance of iron on Mercury's

- surface from MESSENGER X-Ray spectrometer observations. *Icarus* **235**, 170–186.
- Weider S. Z., Nittler L. R., Starr R. D., Crapster-Pregont E. J., Peplowski P. N., Denevi B. W., Head J. W., Byrne P. K., Hauck, II, S. A. and Solomon S. C. (2015) Evidence for geochemical terranes on Mercury: the first global mapping of major elements on the surface of the innermost planet. *Earth Planet. Sci. Lett.* **416**, 109–120.
- Wykes J. L., O'Neill H. St. C. and Mavrogenes J. A. (2015) The effect of FeO on the sulfur content at sulfide saturation (SCSS) and the selenium content at selenide saturation of silicate melts. *J. Petrol.* **56**(7), 1407–1424.
- Yoder H. S. and Tilley C. E. (1962) Origin of basalt magmas: an experimental study of natural and synthetic rock systems. *J. Petrol.* **3**, 342–532.
- Zolotov M. Y., Sprague A. L., Hauck S. A., Nittler L. R., Solomon S. C. and Weider S. Z. (2013) The redox state, FeO content, and origin of sulfur-rich magmas on Mercury. *J. Geophys. Res. Planets* **118**.

Associate editor: Michael J. Toplis